STRAIGHT-IN Dual: a platform for dual, single-copy integrations of DNA payloads and gene circuits into human induced pluripotent stem cells

Albert Blanch-Asensio[1,2,3], Deon S. Ploessl[3], Benjamin B. Johnson[1,2], Sara Cascione[1], Myrthe R. M. Berndsen[1,2], Nathan B. Wang[3], Valeria Orlova[1,2], Anna Alemany[1,2], Christine L. Mummery[1,2], Kate E. Galloway[3,*], Richard P. Davis[1,2,4,*]

[1] Department of Anatomy and Embryology, Leiden University Medical Center, 2300RC Leiden, The Netherlands

[2] The Novo Nordisk Foundation Center for Stem Cell Medicine, reNEW, Leiden University Medical Center

[3] Department of Chemical Engineering, Massachusetts Institute of Technology, MA 02139 Cambridge, USA

[4] Senior author

*Correspondence: katiegal@mit.edu (K.E.G), r.p.davis@lumc.nl (R.P.D)

SUMMARY

Targeting DNA payloads into human (h)iPSCs involves multiple time-consuming, inefficient steps that must be repeated for each construct. Here, we present STRAIGHT-IN Dual, which enables simultaneous, allele-specific, single-copy integration of two DNA payloads with 100% efficiency within one week. Notably, STRAIGHT-IN Dual leverages the STRAIGHT-IN platform to allow near-scarless cargo integration, facilitating the recycling of components for subsequent cellular modifications. Using STRAIGHT-IN Dual, we investigated how promoter choice and gene syntax influence transgene silencing, demonstrating the impact these design features have on reporter gene expression and forward programming of hiPSCs into neurons, motor neurons, and endothelial cells. Furthermore, we designed a grazoprevir-inducible synZiFTR system to complement the widely used tetracycline-inducible system, providing independent, tunable, and temporally controlled expression of different transcription factors within the same cell. The unprecedented efficiency and speed with which STRAIGHT-IN Dual generates homogenous genetically engineered hiPSC populations represents a major advancement for synthetic biology in stem cell applications and opens opportunities for precision cell engineering.

INTRODUCTION

The efficient and precise insertion of DNA payloads into mammalian genome remains a major challenge for synthetic biology, disease modeling, and cell-based therapies. Applications ranging from biosensor and reporter integration to modelling disease variants, generating humanized mouse models, and programming cell fate all require reliable genomic integration tools (Balmas et al., 2023; Blanch-Asensio et al., 2022; Brandão et al., 2020; Hosur et al., 2022; Low et al., 2022; Pawlowski et al., 2017; M. Zhang et al., 2021). Recently, hybrid platforms combining genome editing technologies such as prime editing with site-specific recombinases (SSRs) have enabled the insertion of DNA fragments up to 36 kb, offering a promising route for complex genome engineering (Anzalone et al., 2022; Pandey et al., 2025; Yarnall et al., 2023). However, CRISPR/Cas9-based methods often suffer from off-target effects and variable efficiencies, necessitating extensive clonal screening.

SSR-based methods provide an alternative approach, enabling efficient and high-fidelity integration of large DNA payloads (>100 kb) into engineered landing pad (LP) cassettes (Blanch-Asensio et al., 2022; Brosh et al., 2021; Mitchell et al., 2021; Pinglay et al., 2022). Among these, the serine recombinase Bxb1 is particularly effective due to its high and irreversible integration efficiency, tolerance of large cargoes, and absence of pseudo-recognition sites in the human genome (Duportet et al., 2014; Hosur et al., 2022; Roelle at al., 2023). However, current SSR-based platforms are typically limited to single-copy integration at a single locus. While some platforms permit integration of two DNA payloads (Rosenstein et al., 2024), few support precise, allele-specific insertion of multiple transgenes. Alternative methods, such as cassette exchange which relies on two recombination sites (Matreyek et al., 2017), remain relatively inefficient.

Previously, we developed STRAIGHT-IN, a modular Bxb1-based system for single-copy transgene integration into human induced pluripotent stem cells (hiPSCs) (Blanch-Asensio et al., 2022). Although we also evaluated the recombinase ϕC31 for orthogonal integration of two donor plasmids, its low efficiency in hiPSCs precluded practical use. Recent mechanistic studies of Bxb1 recombination have engineered orthogonal *attP*/*attB* sites by altering the central “GT” dinucleotide to “GA”, which maintained high integration efficiency with minimal crossover between the recombination sequences (Jusiak et al., 2019; Roelle et al., 2023).

Building on these developments and aiming to address limitations of previous systems, we developed STRAIGHT-IN Dual, an hiPSC acceptor line containing two orthogonal Bxb1-compatible LPs. Using a single recombinase, this system enables simultaneous, and allele-specific integration of two DNA payloads into distinct alleles of the *CLYBL* locus, a genomically permissive site that supports stable, long-term transgene expression without perturbing endogenous genes (Cerbini et al., 2015). STRAIGHT-IN Dual also supports seamless removal of auxiliary sequences (e.g. selection markers and vector backbones), using the tyrosine recombinases Cre and Flp. This results in markerless and near-scarless integration of the DNA payload (Blanch-Asensio et al., 2022; Brosh et al., 2021; J. Li et al., 2020), reducing transgene silencing and facilitating iterative genomic modifications.

The dual LP platform facilitates scalable synthetic and stem cell biology studies while controlling for locus-specific and neighboring transgene effects. By enabling single-copy, allele-specific integration of distinct payloads, STRAIGHT-IN Dual supports systematic investigation of how promoter choice, gene syntax (i.e. the relative order and orientation of genes), and other regulatory elements influence transgene expression and stability across pluripotent and differentiated cell states. Moreover, we demonstrated that multiplexed integration of a panel of constructs allows single-pot characterization and identification via Sort-Seq (O'Connell et al., 2023), establishing a scalable framework for high-throughput screening of genetic components, including promoter libraries and synthetic gene circuits.

We further used STRAIGHT-IN Dual to identify optimal strategies for forward programming of hiPSCs into induced neurons (iNs), endothelial cells (iECs), and motor neurons (iMNs), demonstrating that distributing transcription factors across the two LPs enhanced differentiation outcomes. To expand transgene control capabilities, we adapted a grazoprevir-inducible synthetic zinc finger transcription regulator (synZiFTR) system (H.-S. Li et al., 2022) for use in hiPSCs. Combined with the doxycycline-inducible all-in-one Tet-On 3G system, this allowed precise and independent control of dual genetic programs. Notably, we used this to establish dual-fate cell lines in which we could specify distinct fates from a single cell line by applying different inducers, thereby opening opportunities for spatial patterning of multiple cell types from a genetically uniform background.

Taken together, STRAIGHT-IN Dual offers a robust and flexible platform for precise, multi-transgene integration and inducible control in hiPSCs. These capabilities make it uniquely suited for sophisticated cell engineering applications ranging from high-throughput genetic screening to combinatorial circuit design and multi-lineage modeling.

RESULTS

Bxb1 mediates allele-specific integration of two DNA payloads in *CLYBL*

Building upon our previously developed STRAIGHT-IN acceptor hiPSC line that contained a single LP in one allele of *CLYBL* (Blanch-Asensio et al., 2023), we targeted the unedited *CLYBL* allele to establish a dual STRAIGHT-IN acceptor hiPSC line. The original STRAIGHT-IN LP line (LU99_*CLYBL*-bxb-v2) contains a bxb1-GT *attP* site for allele-specific targeting with GT donor plasmids, as well as an excisable fluorescent reporter (*EBFP2*) driven by the PGK promoter and a selection cassette (*BleoR*) designed as a promoter trap due to the lack of an ATG initiation codon and promoter sequence. The 5' and 3' ends of the LP are flanked by two heterospecific *loxP* and *lox257* sites, enabling Cre recombinase (Cre) to excise the auxiliary sequences both 5' and 3' of the payload following integration (**Figure 1**a).

Using TALENs, we targeted a novel LP containing a bxb1-GA *attP* site into the unedited *CLYBL* allele, thereby permitting allele-specific targeting with GA donor plasmids (**Figure 1**a). This bxb1-GA LP also includes a distinct fluorescent reporter (*mScarlet*), selection cassette (*PuroR*) and heterospecific *FRT* and *F3* sites recognized by Flp recombinase. We characterized one of the resulting hiPSC clones (STRAIGHT-IN Dual) expressing mScarlet by genotyping PCR, ddPCR and Sanger sequencing, confirming a single copy of the novel LP in the previously unedited *CLYBL* allele with no mutations in the recombination sites (**Figure 1**b,c and **Supplementary Figure 1**a). Additionally, the genomic integrity and normal karyotypic status of the hiPSC line was confirmed by ddPCR and G-band karyotyping (**Supplementary Figure 1**b,c). The hiPSC clone also expressed pluripotency markers and could differentiate into all three germ layers (**Supplementary Figure 1**d-f).

Next, we designed donor plasmids containing either *attB*-GT or *attB*-GA recombination sites. In the presence of Bxb1, these donor plasmids specifically integrate into their cognate LPs – *attB*-GT into the *attP*-GT allele and *attB*-GA into the *attP*-GA allele – allowing precise allele-specific cargo integrations (**Figure 1**a). Each donor plasmid contains the hEF1a promoter sequence and an ATG initiation codon that completes the promoter trap upon integration, leading to the expression of the respective selection markers (BleoR for the GT allele, PuroR for the GA allele) and conferring resistance to zeocin or puromycin.

We first evaluated the efficiency of GT and GA donor plasmid integration, observing comparable levels for both alleles before selection (1.09% ± 0.21 for GT, 1.10% ± 0.02 for GA; **Figure 1**d,e). Subsequent antibiotic selection led to robust enrichment of hiPSCs containing either the GT or GA donor plasmids (95.52% ± 1.87 for GT, 99.06% ± 0.08 for GA; **Figure 1**d,e). Additionally, co-transfection of both donor plasmids and a Bxb1 expression plasmid, followed by dual antibiotic selection, resulted in >93.9% of hiPSCs containing both integrated payloads (**Supplementary Figure 1**g,h).

To confirm allele specificity, we independently transfected either the GT or GA donor plasmids and subjected cells to selection with the non-matching antibiotic. If the GT donor incorrectly integrated into the *attP*-GA LP, puromycin resistance would be conferred. Likewise, incorrect GA donor integration into the GT LP would lead to zeocin resistance (**Figure 1**f). In both cases, selection resulted in complete cell death, confirming the orthogonality of the alleles (**Figure 1**f).

To further validate the orthogonality of the GT and GA alleles, we cloned green and red fluorescent reporters (*TurboGFP* and *mScarlet-I*, respectively) into both donor plasmids (**Figure 1**g). *TurboGFP* was tagged with a nuclear localization sequence (NLS), and *mScarlet*-I with an actin-targeting signal, enabling unambiguous visualization of each transgene within individual cells. As expected, co-transfection of the two fluorescent payloads targeting the same LP (either *attP*-GT or *attP*-GA) resulted in cells expressing only one fluorophore, consistent with mutually exclusive integration. In contrast, co-transfection of *TurboGFP*-GT and *mScarlet-I*-GA donor plasmids yielded dual-labeled hiPSCs (**Figure 1**g). No integration was observed when the *TurboGFP*-GA donor was transfected into the parental *CLYBL*-bxb-v2 hiPSC line which lacks the GA allele, further supporting allele specificity and excluding detectable off-target integration (**Supplementary Figure 1**i). Finally, integrating the same fluorescent reporter into both LPs resulted in an ~2-fold increase in fluorescence signal, suggesting that both *CLYBL* alleles support comparable levels of transgene expression (**Supplementary Figure 1**j).

Accelerating and simplifying the STRAIGHT-IN Dual protocol improves cell line generation

To streamline the generation of uniform, genetically modified hiPSCs, we optimized the STRAIGHT-IN integration process to improve efficiency, increase cell yield, and shorten the

time before downstream experiments could be performed (**Figure 2**a). We hypothesized that the lower cytotoxicity and higher transgene expression typically observed with modRNA delivery compared to plasmid DNA in hiPSCs would improve integration outcomes. Indeed, transfection of Bxb1 modRNA resulted in an approximate 2-fold increase in integration efficiency (**Supplementary Figure 2**a).

Next, we explored whether co-delivery of cytoprotective factors could improve post-transfection survival, as reported for CRISPR-based genome editing (Haideri et al., 2022, 2024). Co-transfection of *p53DD* modRNA increased the proportion of hiPSCs with an integrated cargo by 12.4-fold compared to a control *mGreenLantern* modRNA (**Supplementary Figure 2**b). We also evaluated four engineered Bxb1 variants with reported improvements in recombination activity (Hew et al., 2024; Pandey et al., 2025), namely evoBxb1 (V74A), eeBxb1 (V74A + E229K + V375I), Bxb1-I87L, and Bxb1-I87L + A369P + E434G. Among these, eeBxb1 delivered as modRNA, and combined with p53DD modRNA, significantly increased pre-selection integration efficiency from 2.75% to 9.12% at the GT allele, and from 1.46% to 11.7% at the GA-allele (**Figure 2**b). Other Bxb1 variants did not outperform wildtype Bxb1, although co-transfection of *p53DD* modRNA consistently improved integration efficiencies across all experiments (**Supplementary Figure 2**c).

Based on these optimization experiments, and to expedite enrichment with zeocin or puromycin, we used modRNA for all subsequent donor plasmid integrations. Because modRNA results in more rapid Bxb1 expression than via plasmid delivery, antibiotic selection could begin one day after transfection. This reduced the time required to obtain uniform, payload-carrying hiPSCs to less than one week (**Figure 2**c,d). Notably, inclusion of *p53DD* modRNA enabled recovery of hiPSC colonies with both GT and GA integrations after only 3 days of antibiotic selection (**Figure 2**e, **Supplementary Figure 2**d). ddPCR confirmed single-copy insertions of the GT and GA donor plasmids, with no evidence of random integration (**Supplementary Figure 2**e).

After integration, Cre and Flp recombinases are used to excise auxiliary elements, leaving behind only the DNA payload and often improving integrated transgene expression (**Figure 2**f)(Blanch-Asensio et al., 2022). While plasmid-based recombinase expression can result in high excision rates with selection, it often results in few clones surviving and prolonged

expansion times. To improve this, we explored plasmid-free strategies using either modRNA or recombinant protein delivery.

For the GT allele, delivery of TAT-Cre protein resulted in excision rates of 91.9% and 80.7% of the *loxP*- and *lox257*-flanked sequences, respectively. A second round of TAT-Cre increased this to 97.6% and 93.7% (**Figure 2**g). For the GA allele, where TAT-Flp protein is unavailable, we used *Flp* modRNA. After one transfection, 61.5% and 54.8% of the hiPSCs had excised the *FRT*- and *F3*-flanked sequences, respectively, increasing to 87.8% and 76.3% with a second transfection (**Supplementary Figure 2**f, *left*). Co-delivery of *TAT-Cre* and *Flp* modRNA resulted in 83.6% of hiPSCs excising all flanked auxiliary sequences after two transfection rounds (**Supplementary Figure 2**f, *right*).

We hypothesized that coupling excision to selection might further enhance efficiency, potentially enabling complete removal of auxiliary elements after a single transfection. To test this, we integrated a donor plasmid into the GA allele, conferring puromycin resistance but keeping the cells zeocin sensitive. Transfecting a modRNA encoding both Flp and BleoR (*Flp-2TA-BleoR*), followed by zeocin selection starting one day later, resulted in nearly complete excision of both upstream and downstream auxiliary elements within 3 days with efficiencies of 99.3% and 97.2%, respectively (**Figure 2**h). However, an equivalent strategy could not be replicated with Cre for donor plasmids integrated at the GT allele, as puromycin selection following *Cre-T2A-PuroR* or *Cre-IRES-PuroR* modRNA transfection failed to yield puromycin-resistant hiPSCs. Co-transfection of *Cre* and *PuroR* modRNAs resulted in limited excision enrichment, with efficiencies only increasing from 25.7% to 44.3% for *loxP*- and from 22.5% to 41.7% for *lox257*-flanked sequences (**Supplementary Figure 2**g).

Finally, to further streamline the protocol, we performed donor plasmid integration and auxiliary element excision in the same well without needing to passage the cells. The hiPSCs were co-transfected with *eeBxb1* and *p53DD* modRNA along with a GA donor plasmid encoding *EGFP*, followed by puromycin selection days 1-3 post-transfection. On day 4, y *Flp-T2A-BleoR* modRNA was transfected, and zeocin selection applied from days 5-8 (**Figure 2**i). Within 9 days, hiPSCs showed near uniform EGFP expression and excision of auxiliary elements (**Figure 2**j,k), demonstrating a rapid, one-well protocol for precise, near-scarless single-copy genome integration with >98% efficiency.

Identifying promoter sequences supporting stable transgene expression in hiPSCs

Transgenes are essential tools for tracking cellular processes and modulating cell behavior and identity (Peterman et al., 2024). However, in hiPSCs, genome-integrated transgenes are susceptible to transcriptional silencing, particularly during prolonged culture or upon differentiation. Promoter choice plays a critical role in determining both expression strength and silencing susceptibility (**Figure 3**a)(Cabrera et al., 2022; Seczynska et al., 2022). Although the CMV early enhancer/chicken β-actin (CAG) and human elongation factor 1-alpha (hEF1a) promoters are commonly used for constitutive transgene expression across diverse cell types (Dou et al., 2021), their comparative activity in hiPSCs remains poorly defined.

To directly compare their activity, we generated a dual reporter hiPSC line in which divergently oriented CAG and hEF1a promoters drove expression of *mRuby2* and *mGreenLantern*, respectively. While all puromycin-resistant hiPSC colonies showed uniform mRuby2 expression, only a subset expressed mGreenLantern despite confirmed integration of the hEF1a-driven cassette, indicating transcriptional silencing. This effect became more pronounced with passaging (**Supplementary Figure 3**a).

To exclude reporter-specific effects and promoter interference, we replaced *mGreenLantern* with *mStayGold*, the brightest monomeric GFP reported to date (H. Zhang et al., 2024). Additionally, we integrated the two reporters into separate *CLYBL* alleles. Again, only the hEF1a-driven mStayGold was silenced (**Supplementary Figure 3**b). Swapping promoter-reporter pairs also confirmed this, with strong expression of CAG-driven mStayGold while hEF1a-driven mRuby2 was silenced (**Supplementary Figure 3**c).

We next screened a panel of 11 promoters to identify sequences capable of driving low, medium, or high levels of transgene expression. In addition to hEF1a and CAG, the panel included ubiquitous promoters (UbC, β-actin, PGK), viral (CMV, RSV, SV40) promoters, truncated CAG variants (CBh, shortCAG), and CpG-depleted hEF1a variant (CpG-free). We introduced the promoters either separately or in a multiplexed format to demonstrate the feasibility of integrating plasmid libraries using STRAIGHT-IN. This also enabled direct comparison of pooled versus individual outcomes (**Figure 3**b). While all promoters initially produced detectable mStayGold expression 24 h after transfection, their expression profiles diverged markedly following single-copy genomic integration at the *CLYBL* locus, indicating

potential context-dependent differences between episomal and integrated transgene expression (**Supplementary Figure 4**a,b).

Among the candidates tested, full-length CAG consistently supported the strongest expression of mStayGold, followed by its truncated derivative CBh. The UbC and β-actin promoter sequences produced intermediate and low expression levels respectively, suggesting their potential utility in applications requiring tighter control. In contrast, the remaining promoters, including hEF1a, CMV, and CpG-free, either failed to promote homogenous mStayGold expression or were rapidly silenced upon passaging (**Figure 3**c). Longitudinal monitoring over ten passages showed sustained mStayGold expression from CAG and UbC promoters, while with hEF1a it remained silenced in most cells (**Supplementary Figure 4**c).

We next evaluated promoter behavior in a pooled context. All 11 promoter constructs were detected in the bulk population by next generation sequencing (**Supplementary Figure 4**d). Cells were then binned into four mStayGold-based expression clusters (negative, low, medium, and high), and the specific promoter sequences in each sorted cluster were mapped (**Figure 3**d,e and **Supplementary Figure 4**e). The expression patterns closely matched those from individually integrated lines, with CAG and CBh enriched in the high expression cluster, UbC in the intermediate, β-actin in the low, and hEF1a, PGK and the remaining promoters predominantly appearing in the negative cluster.

To assess whether these results were locus dependent, we integrated 6 of the promoter constructs (hEF1a, CAG, UbC, CBh, β-actin, PGK) into a hiPSC line containing a STRAIGHT-IN LP at the *AAVS1* locus (Blanch-Asensio et al., 2023) (**Supplementary Figure 5**a). As observed at the *CLYBL* locus, CAG again drove strong and stable transgene expression across multiple passages at *AAVS1*, whereas constructs containing hEF1a and PGK underwent silencing (**Supplementary Figure 5**b). Notably, UbC, CBh and β-actin displayed greater variability in both silencing and expression levels between the two loci, indicating that both the promoter and locus influence the stability and strength of transgene expression.

These findings guided further optimization of the STRAIGHT-IN donor plasmids. Since CAG consistently supported strong and stable transgene expression and hEF1a was more prone to silencing, we designed the GT and GA donor plasmids to place the CAG promoter upstream

of the transgene cloning site (**Supplementary Figure 6**a). Additionally, as the original GA donor plasmid relied on hEF1a to drive *PuroR* expression in the LP, we hypothesized that this might limit the recovery of puromycin-resistant colonies. To test this, we replaced hEF1a with CAG, UbC or CBh (**Supplementary Figure 6**b). Following puromycin selection, we observed 1.45x, 2.29x and 3.84x increases in the colony numbers respectively, indicating that poor hEF1a activity was impairing selection efficiency (**Supplementary Figure 6**c).

Gene syntax influences induction efficiency in the Tet-On 3G system in hiPSCs

Beyond promoter selection, the relative arrangement of transcriptional units, often referred to as gene syntax, can influence the expression of adjacent genes (Engreitz et al., 2016; Johnstone & Galloway, 2022; Patel et al., 2023). While placing different elements of genetic circuits, such as inducible systems, at separate genomic loci may prevent suboptimal interactions between genes, integration at separate sites also requires integrating additional genetic cargo. To systematically compare how different designs of multi-component genetic circuits perform, we used STRAIGHT-IN Dual to elucidate key design principles, focusing on the Tet-On 3G system and examining trade-offs between co-localized and dual locus integration.

We first constructed a *trans* design of the Tet-On 3G system, with the transcriptional units integrated into the separate *CLYBL* alleles (**Figure** 4a). The inducible gene (*mScarlet*) was driven by a tetracycline response element (TRE) containing seven tetracycline operator (*TetO*) repeats. Having determined the CAG promoter resists silencing in hiPSCs, we used this promoter to drive expression of the transactivator gene *rtTA* in a bicistronic cassette which also expressed a nuclear-localized blue fluorescent reporter (*mTagBFP2-NLS)* as a proxy readout for rtTA levels.

We also generated *cis* designs of the Tet-On 3G system, where both the constitutive (*rtTA-T2A-mTagBFP2-NLS*) and inducible (*mScarlet*) transcriptional units were integrated into the same allele. This allowed us to investigate how gene syntax, specifically the relative orientation and order of the transcriptional units, affects induction. We created four possible syntaxes: convergent, divergent, downstream tandem and upstream tandem (**Figure 4**a). As the auxiliary sequences remaining in the GA allele could confound potential interactions between the constitutive and inducible genes due to the presence of two copies of mScarlet,

we examined mTagBFP2 and mScarlet expression both before (**Supplementary Figure 7**) and after excision of the sequences (**Figure 4**).

In the *trans* configuration, induced mScarlet expression was weak, whereas several *cis* designs showed robust induction (**Figure 4**b), suggesting that spatial proximity between the constitutive and inducible genes improves expression in the Tet-On 3G system. Notably, *mTagBFP2* expression levels remained unchanged in the *trans* configuration, indicating that resource burden was not a limiting factor in induction (**Figure 4**c,d).

Prior to induction, we observed clear bimodality in mTagBFP2 expression for the convergent syntax, which was most pronounced in unexcised cells (**Supplementary Figure 7**c), and aligned with biophysical models of transcription (Johnstone & Galloway, 2022). In contrast, the other syntaxes exhibited unimodal mTagBFP2 expression, which remained stable upon induction with 1 µM doxycycline (**Supplementary Figure 7**c). Interestingly, in pre-excised cells, induction resulted in slight repression of mTagBFP2 across all syntaxes (**Supplementary Figure 7**d). However, after excision, syntax-specific differences in mTagBFP2 expression emerged (**Figure 4**c,d). Most notably, the downstream tandem syntax exhibited an ~5-fold reduction in mTagBFP2 expression, while the convergent syntax showed no significant change. The divergent and upstream tandem syntaxes showed increased mTagBFP2 expression, in line with biophysical model predictions (**Figure 4**c,d).

Upon induction with 1 µM doxycycline, striking syntax-specific differences also emerged in mScarlet expression. Although these differences became more pronounced after excision (**Figure 4**b-d), similar trends were observed before excision (**Supplementary Figure 7**e,f). The divergent and downstream tandem syntaxes resulted in strong mScarlet induction, while the convergent and upstream tandem syntaxes showed poorer induction, characterized by weak, bimodal, or broad expression distribution. Interestingly, excision significantly improved induction for the convergent syntax, possibly due to the increased expression of mTagBFP2 and therefore rtTA. However, excision did not improve induction for the upstream tandem syntax (**Figure 4**c,d).

Given the robust mScarlet induction observed in the downstream tandem *cis* design, we further explored its utility in 3D stem cell-derived cardiac organoids (cardioids), which provide a more complex cellular environment for disease modeling and developmental studies. We

found that mScarlet expression could be modestly adjusted by varying doxycycline concentration (**Figure 4**e). Additionally, altering the duration of doxycycline treatment modulated mScarlet expression, with longer inductions leading to higher expression (**Figure 4**f). Even in developed cardioids, robust mScarlet expression could be achieved when adding doxycycline from day 7, demonstrating the potential to dynamically modulate transgene expression in complex 3D systems.

Dual payload inducible system enables forward programming of hiPSCs into iNs and iMNs

Forward programming of hiPSCs into specific cell types is typically achieved by overexpressing lineage-defining transcription factors. However, suboptimal gene syntax may impair transcription factor expression and thereby inhibit cell fate conversion (**Figure 5**a). Given the striking differences we observed between the two tandem orientations (**Figure 4**d), we investigated whether gene syntax also influenced forward programming outcomes when overexpressing *Ngn2,* a pioneer transcription factor for neurons (Y. Zhang et al., 2013). To evaluate this, we constructed Tet-On 3G all-in-one systems for regulating Ngn2 expression.

To enable rapid cloning of *Ngn2* and other genes of interest (GOIs) into the STRAIGHT-IN LPs, we developed a modular set of tandem and divergent Tet-On 3G donor plasmids (**Supplementary Figure 8**a). These vectors included a constitutive nuclear BFP reporter for visualization and a LacZ cassette to facilitate blue/white screening of bacterial colonies containing the cloned inserts. After assembly, >85% of white colonies carried the correct cargo (**Supplementary Figure 8**b,c). This streamlined workflow allowed rapid generation of donor plasmids with diverse inducible cargoes and, using the rapid integration protocol, the establishment within 1 week of hiPSC lines that uniformly expressed the nuclear BFP reporter (**Supplementary Figure 8**d,e).

Induction of *Ngn2* from the downstream tandem syntax led to the rapid generation of $TUJ1^+$ $MAP2^+$ hiPSC-derived iNs within 7 days (**Figure 5**b and **Supplementary Figure 9**a). In contrast, the upstream tandem configuration produced very few iNs (**Figure 5**c), consistent with its weaker expression profile observed earlier (**Figure 4**c,d). qPCR analysis confirmed reduced induction of *Ngn2* and other neuronal genes in the upstream tandem syntax, while

pluripotency-associated genes were downregulated in the downstream tandem orientation following doxycycline induction (**Figure 5**d).

To demonstrate the utility of STRAIGHT-IN Dual for co-expressing multiple transgenes, we integrated *Ngn2* and a genetically encoded calcium indicator (*jRCaMP1b*) into the separate *CLYBL* alleles using two TRE-controlled donor plasmids (**Supplementary Figure 9**b). With doxycycline as a single inducer, this configuration resulted in rapid and robust forward programming of hiPSCs into iNs while simultaneously allowing the monitoring calcium signals (**Supplementary Figure 9**c-e), illustrating how the Dual system enables the coupling of lineage conversion with real-time functional readouts.

We next investigated whether distributing the transcription factors required for motor neuron (iMN) specification (*Ngn2*, *ISL1* and *LHX3*) across both LPs would improve the homogeneity of forward programming outcomes. Specifically, we compared a dual-cassette configuration in which *Ngn2* and the *ISL1/LHX3* cassette were integrated separately (GT-Ngn2 + GA-ISL1-LHX3; GT-N + GA-IL) to a single-cassette configuration where all three factors were encoded in tandem within a single LP (GT-Ngn2-ISL1-LHX3; GT-NIL; **Figure 5**e). The single-cassette GT-NIL configuration led to a high proportion of proliferative, non-neuronal cells that rapidly overtook the culture (**Supplementary Figure 9**f). In contrast, the dual-cassette strategy resulted in improved neuronal differentiation, yielding a purer population of iMNs (**Supplementary Figure 9**f). While in the single-allele approach, the non-neuronal cells were selectively eliminated by treatment with the antimitotic reagent EdU, this step was not required for the dual-cassette design (**Supplementary Figure 9**g,h).

After 10 days of differentiation, live-cell imaging with Hoechst and propidium iodide showed increased cell death in EdU-treated single-cassette cultures, consistent with the higher proportion of non-neuronal, EdU-sensitive cells (**Supplementary Figure 10**a-d). Additionally, calcein AM staining and image quantification revealed that cells derived from the dual-cassette configuration were significantly larger, exhibited increased neurite branching, and had longer dendrites (**Supplementary Figure 10**a-d). Furthermore, qPCR confirmed that expression of *Ngn2*, *ISL1*, and *LHX3* was lower in the single-cassette configuration, while the dual-cassette cultures showed robust upregulation of motor neuron markers, including HB9, ChAT and VaChT, compared to *Ngn2* alone (**Supplementary Figure 10**e).

To evaluate the effect of copy number, allele configuration (cis versus trans), and transcript architecture, we generated 3 additional lines. First, to separate the effect of the tricistronic cassette while maintaining expression from a single allele, we expressed the transcription factors either as three separate inducible transcription units in a downstream tandem orientation (GA-N+I+L D-Tand), or as two units in a divergent syntax with one encoding *Ngn2* and the other carrying a bicistronic *ISL1–LHX3* cassette (GA-N+IL Div; **Supplementary Figure 11**a,b). To investigate whether expression of the transcription factors from the tricistronic NIL cassette could be increased, we introduced a second identical copy into the GA allele of the GT-NIL line (GT-NIL + GA-NIL; **Figure 5**e). As expected, dual integration resulted in an approximately two-fold increase in *mTagBFP2* expression (**Figure 5**f), and after three days of doxycycline induction this line exhibited the highest levels of all three transcription factors among the six lines analyzed (**Supplementary Figure 11**c).

By day 10 of differentiation, cell morphology and qPCR analysis of motor neuron genes indicated more robust motor neuron differentiation in the two dual-allele lines (GT-N+GA-IL and GT-NIL+GA-NIL), consistent with their elevated transcription factor expression (**Figure 5**g and **Supplementary Figure 11**d,e). Immunofluorescence staining for HB9 further confirmed motor neuron identity (**Figure 5**h and **Supplementary Figure 11**f). Quantification of $HB9^+$ nuclei relative to total $DAPI^+$ nuclei showed that >85% of cells in the GT-N+GA-IL line expressed HB9 at day 10, whereas approximately 40% of cells were $HB9^+$ in the dual GT-NIL+GA-NIL line and <20% in the remaining lines (**Figure 5**i and **Supplementary Figure 11**g. Altogether, these data suggest that the single-transcript design may impede effective differentiation by limiting transcription factor expression. While increasing copy number improved both expression and differentiation, this alone did not achieve a differentiation efficiency similar to the split-allele design of the GT-N+GA-IL line.

Rapid generation of hiPSC-iECs and promoter activity profiling in differentiated lineages using STRAIGHT-IN Dual

To further demonstrate the versatility and efficiency of our all-in-one Tet-On 3G downstream-tandem vector system for generating inducible hiPSC lines, we cloned and overexpressed *ETV2*, a pioneer transcription factor that directs endothelial lineage specification (**Supplementary Figure 12**a). Upon doxycycline induction, cells rapidly acquired an

endothelial-like morphology and, by day 4, expressed key markers of endothelial identity, including CD31, ZO1, and CD144 (**Supplementary Figure 12**b-d).

To evaluate promoter activity following lineage commitment, we integrated the previously characterized panel of 11 promoters into the GA allele of hiPSC lines harboring doxycycline-inducible *Ngn2* or *ETV2* in the GT allele. This enabled side-by-side comparison of promoter activity in iNs and iECs, as well as hiPSCs (**Supplementary Figure 13)**.

Promoter behavior in iNs and iECs largely mirrored that observed in undifferentiated hiPSCs. As in the pluripotent state, the CAG promoter drove strong and uniform mStayGold expression in both iNs and iECs (**Supplementary Figure 13**b,c). Similarly, the UbC and β-actin promoters also remained active, producing moderate and low levels of reporter expression, respectively. In contrast, the remaining promoters, including hEF1a, PGK and CBh, either failed to produce detectable reporter signals or exhibited transgene silencing, consistent with observations in undifferentiated hiPSCs.

Orthogonal inducible systems support dual-fate programming of genetically uniform hiPSCs

To achieve independent control over two separate cargoes within a single hiPSC line, we introduced a second, orthogonal inducible system alongside the Tet-On 3G system. We selected a synZiFTR system which couples ZF10 as a DNA-binding domain to a grazoprevir (GZV)-responsive NS3 module and a p65 transcriptional activator (H.-S. Li et al., 2022). An all-in-one synZiFTR expression cassette was constructed in the downstream tandem configuration and integrated into the GA allele (**Supplementary Figure 14**a,b). Induction of a *mGreenLantern* reporter revealed toxicity at GZV concentrations above 250 nM, with 125 nM selected as the optimal concentration for robust transgene induction with minimal cytotoxicity (**Supplementary Figure 14**c). At this concentration, synZiFTR-mediated Ngn2 expression efficiently generated $TUJ1^+/MAP2^+$ iNs within 7 days (**Figure 6**a,b).

To demonstrate independent dual gene regulation, we combined both inducible systems using STRAIGHT-IN Dual. *Ngn2* was integrated into the GA allele under synZiFTR control, while mScarlet was targeted to the GT allele under Tet-On 3G regulation (**Figure 6**c). GZV was maintained in the culture media throughout the 7-day differentiation procedure, with doxycycline added from day 3. By day 7, most iNs expressed mScarlet (**Figure 6**d and **Supplementary Figure 14**d).

To exploit this modularity, we established dual-fate hiPSC lines capable of differentiating into distinct lineages based on inducer choice. In one configuration, *Ngn2* expression was controlled by the synZiFTR system and *ETV2* by Tet-On 3G, while in another, this arrangement was reversed (**Figure 6**e). Exposure to GZV or doxycycline resulted in rapid and efficient differentiation into either iNs or iECs (**Figure 6**f). Lineage-specific commitment was supported by qPCR analysis and flow cytometry, with GZV-induced iECs expressing CD31 and CD144 (**Figure 6**g and **Supplementary Figure 12**e). These findings highlight the versatility of STRAIGHT-IN Dual for independently controlling multiple transcriptional programs in a single, genetically uniform hiPSC line. This capability provides a flexible framework for implementing orthogonal gene circuits and generating mixed or patterned cell populations for advanced applications.

DISCUSSION

In this study, we present STRAIGHT-IN Dual, a platform enabling rapid, efficient, and allele-specific integration of two independent DNA payloads into the *CLYBL* locus in hiPSCs. Following protocol optimization, genetically modified hiPSC lines could be generated in less than one week with nearly 100% efficiency. For the GA allele, both integration and excision procedures were achievable within nine days without requiring cell passaging.

STRAIGHT-IN Dual supports simultaneous integration of two payloads with orthogonal precision, exploiting the highly specific GT and GA Bxb1 recombination sequences (Jusiak et al., 2019). By using eeBxb1, a hyperactive Bxb1 mutant developed via directed evolution (Pandey et al., 2025), we achieved significantly higher integration efficiencies compared to wild-type Bxb1. Notably, this improvement was more pronounced at the GA allele. This may be due to the attP/attB-GA sequence being included in some of the circuits used during the directed evolution of Bxb1 to eeBxb1 (Pandey et al., 2025), potentially biasing the enzyme toward enhanced recombination at these sites. However, the precise mechanism by which the central dinucleotide sequence influences recombination efficiency remains unclear and requires further investigation.

Since Bxb1 catalyzes recombination through DNA double-strand breaks (Xu et al., 2013), we also investigated whether co-delivering modRNA encoding a dominant-negative truncated p53 (p53DD) to dampen the p53-mediated DNA damage response would enhance cell survival after recombination (Haideri et al., 2024; M. Li et al., 2022; Rosenstein et al., 2024). Combining eeBxb1 and p53DD resulted in approximately a 10-fold increase in integration efficiency.

The platform also supports near-scarless genomic modifications by excising auxiliary elements, such as reporters, selection markers, and plasmid backbones. Consistent with prior findings (Blanch-Asensio et al., 2024), removal of these auxiliary sequences reduced transgene silencing in both undifferentiated and differentiated hiPSCs. Excision also allows reuse for further genomic modifications. STRAIGHT-IN Dual facilitated near-complete excision efficiency from both alleles using TAT-Cre and *Flp-T2A-BleoR* modRNA, with the entire procedure for the GA allele achieved without cell passaging. This streamlined approach simplifies the generation of multiple modified hiPSC lines, either individually or pooled,

facilitating integration of plasmid libraries and high-throughput combinatorial studies at single-copy resolution. These optimized processes also make STRAIGHT-IN Dual compatible with automated pipelines, making it ideal for large-scale functional screens and high-throughput studies.

Importantly, dual integration of the same payload into both alleles effectively doubled transgene expression, indicating that both LPs perform comparably. We recently demonstrated that such uniform biallelic integration is critical for high-resolution genome folding profiling and enables precise measurements of transcriptional activation effects on chromatin architecture using Region Capture Micro-C (Johnstone et al., 2025).

Our work also highlights current limitations of standard molecular tools used in hiPSCs. For example, the commonly used hEF1a promoter was rapidly silenced, corroborating earlier studies (Bertero et al., 2016). To identify promoter sequences that resist silencing, we screened a library of 11 promoters integrated either individually or as a pool into STRAIGHT-IN Dual hiPSCs. Next-generation sequencing of pooled integrations confirmed complete library representation, demonstrating the suitability of STRAIGHT-IN for scalable, high-throughput characterization of diverse DNA elements.

While transient assays initially showed detectable transgene expression from all promoters, over half underwent significant silencing following genomic integration. Viral promoters (CMV, RSV, SV40), a truncated CAG promoter variant (shortCAG), and a CpG-depleted short hEF1a promoter (CpG-free) were silenced rapidly, while PGK and hEF1a promoters showed progressive silencing over time. In contrast, CAG, CBh, UbC, and β-actin promoters maintained stable reporter expression at the *CLYBL* locus over extended passaging in hiPSCs, although only CAG maintained long-term activity at the *AAVS1* locus. When assessed in forward programmed neurons and ECs, most promoter behaviors mirrored that in undifferentiated hiPSCs. Notably, CAG, UbC, and β-actin promoters remained active, supporting their utility for stable gene expression in cell types derived from different germ layers.

The superior stability of the full-length CAG promoter likely arises from its synthetic architecture, which integrates several regulatory elements that collectively confer resistance to transcriptional silencing. CAG combines the cytomegalovirus (CMV) immediate-early

enhancer, the chicken β-actin promoter with its first intron, and a rabbit β-globin splice acceptor (Niwa et al., 1991). These elements contain numerous transcription factor binding sites, can recruit chromatin remodelers and prevent DNA methylation (Brown et al., 2014). In contrast, truncated variants such as CBh, shortCAG, and CMV alone, lack at least the β-globin splice acceptor, and showed reduced resistance to silencing. Nonetheless, the large size and high GC content of CAG presents practical cloning challenges, highlighting the need to systematically develop and evaluate alternative synthetic promoters that retain the robust, stable expression characteristics of CAG but offer improved ease of use. STRAIGHT-IN Dual offers not only rapid, locus-controlled screening of promoter sequence libraries but also the possibility to evaluate other regulatory elements, such as insulators or ubiquitous chromatin opening elements, that have been proposed to mitigate transgene silencing in hiPSCs and their differentiated derivatives (Uenaka et al., 2025; Yanagi et al., 2025; Guichardaz et al., 2024).

We also demonstrated the utility of STRAIGHT-IN Dual for systematically analyzing gene syntax, identifying divergent and downstream tandem orientations as optimal configurations for induction with the all-in-one Tet-On 3G system. Most studies have favored these two orientations in mammalian cells (Jillette et al., 2019; Kelkar et al., 2020; Ng et al., 2021; Otomo et al., 2023; Randolph et al., 2017), with convergent and upstream tandem syntaxes typically performing poorly unless extensively optimized (Haenebalcke et al., 2013; Shin et al., 2024).

Based on the clear differences in expression observed between the two tandem syntaxes, we evaluated both for forward programming of hiPSCs into iNs via inducible *Ngn2* expression. We selected the downstream tandem syntax over the divergent orientation due to its higher transgene induction levels prior to excising the flanking auxiliary elements, thereby obviating the need to perform this step and allowing the initiation of overexpression studies within one week. Functional iNs were only obtained when using the downstream tandem syntax, confirming its superior performance which is consistent with an upstream dominance effect driven by supercoiling-mediated feedback that regulates the expression of neighboring genes in a syntax-specific manner (Johnstone et al., 2025). The downstream tandem syntax also proved effective for *ETV2* overexpression, enabling efficient differentiation of hiPSCs into iECs within four days. While similar outcomes have been reported previously, these studies relied on hyperactive transposase-based delivery systems that randomly inserted >50 copies of the

construct throughout the genome and potentially led to unintended genomic disruption (Rieck et al., 2024; Ding et al., 2025). In contrast, we demonstrate that a single, site-specific integration of *ETV2* is sufficient to forward program the entire hiPSC population into iECs and suggests that high transgene copy numbers are not a prerequisite for rapid and uniform cell fate specification when expression is tightly controlled.

Our comparative analysis of transcription factor cassette configurations demonstrates that transcript architecture and allelic arrangement strongly influence both expression efficiency and downstream motor neuron differentiation. Neither the downstream tandem orientation with three separate inducible transcription units nor the divergent bicistronic design increased transcription factor output or improved conversion of hiPSCs into iMNs, indicating that simply reorganizing transcriptional units is insufficient to overcome intrinsic expression constraints imposed by the single tricistronic NIL cassette (Wang et al., 2025). Introducing a second NIL cassette into the other allele increased overall expression as expected, confirming that copy number contributes in a predictable manner to transcriptional output. However, despite this improvement, the dual NIL configuration did not achieve differentiation efficiencies comparable to the split-allele GT-N+GA-IL design. The GT-N+GA-IL line, which distributes a single copy of the transcription factors across two alleles, consistently showed superior induction of motor neuron markers and the highest proportion of $HB9^+$ cells, possibly because it avoids position effects common to 2A-linked polycistronic constructs (Liu et al., 2017). Future work may identify improved design strategies for multicistronic cassettes that overcome these limitations. More broadly, STRAIGHT-IN Dual enables systematic screening of transcription factor combinations for lineage specification, which has previously largely relied on pooled viral strategies that offer limited control over transcription factor stoichiometry (Joung et al., 2023; Ng et al., 2021).

Moreover, STRAIGHT-IN Dual allows combinatorial or sequential transgene expression using independent inducible systems, such as Tet-On 3G and synZiFTRs. This enabled precise temporal control of both reporters and lineage-specifying transcription factors. Using this dual-inducible framework, we generated dual-fate programmable hiPSC lines that could be directed toward either neuronal or endothelial lineages, depending on inducer choice. Previous multi-fate approaches have relied on mixing or printing genetically distinct cell populations (Skylar-Scott et al., 2022). In contrast, our strategy enables spatial patterning of

distinct lineages from a single cell line using small molecules alone, without the need for complex bioprinting. The platform also opens possibilities to combine cell fate programming with independent expression of biosensors or inducible modeling of sporadic or acquired mutations in differentiated cells. Furthermore, these inducible DNA payloads can be expressed in complex in vitro systems, such as organoids, organs-on-chips, and 3D tissue constructs, expanding the possibilities for cell-based modelling and engineered tissue design.

Several limitations of the current study should be acknowledged. First, all engineered hiPSC lines were derived from a single parental clone. Although beneficial for reducing variability, this genetic uniformity limits the immediate generalizability of our findings. Further validation using hiPSC lines from diverse genetic backgrounds and donors is therefore warranted, with STRAIGHT-IN Dual LPs currently being targeted in additional hiPSC lines. Second, most payloads were integrated into the *CLYBL* locus, with limited comparisons at *AAVS1*. Therefore, locus-specific effects cannot be excluded, and transgene behavior could differ across genomic sites. Third, the transgene sequence also influences transgene silencing (Karbassi et al., 2024). Here, promoter activity was primarily assessed using fluorescent reporter genes. Further testing of promoter activity for a broader range of relevant payloads is warranted in future studies.

In summary, STRAIGHT-IN Dual enables the rapid generation of complex, precisely engineered hiPSC lines with dual, orthogonal genetic control. This versatile platform supports scalable screening, combinatorial transgene interrogation, and precise control of cell fate, and provides a powerful toolkit for biomedical and synthetic biology research.

ACKNOWLEDGEMENTS

We thank Niels Geijsen and Peng Shang for providing TAT-Cre protein, the LUMC flow cytometry facility for sorting the cells, and the Laboratory for Diagnostic Genome Analysis (LUMC) for karyotyping. Some schematics in figures were created with BioRender.com. This work was supported by the Netherlands Organ-on-Chip Initiative, a Gravitation project of the Nederlandse Organisatie voor Wetenschappelijk Onderzoek (NWO), funded by the Ministry of Education, Culture, and Science of the government of the Netherlands (grant no. 024.003.001); the NWO-funded LymphChip project (grant no. NWAORC 2019 1292.19.019)

as part of the NWA research program ‘‘Research on Routes by Consortia (ORC)’’; funding from the NWO Open Competition XS program (grant no. OCENW.XS23.4.123); a ZonMw PSIDER consortium grant (grant no. 10250022120002; GREAT); and a Marie Sklodowska-Curie fellowship (grant no. 101152209) under the European Union’s Horizon 2020 research and innovation program. It also forms part of the project “Innovative Stem Cell Technology Infrastructure for Human Organ and Disease Models”, funded by the NWO Large-Scale Research Infrastructure program (grant no. 184.036.006). The Novo Nordisk Foundation Center for Stem Cell Medicine (reNEW) is supported by a Novo Nordisk Foundation grant (NNF21CC0073729). Additional support was provided by the National Institute of General Medical Sciences of the National Institutes of Health (award no. R35-GM143033 to K.E.G), the National Science Foundation under the NSF-CAREER award (grant no. 2339986), and with funding from Institute for Collaborative Biotechnologies (W911NF-19-2-0026), by the Air Force Research Laboratory MURI (FA9550-22-1-0316), and the Pershing Square Foundation MIND Prize. This study also received funding from European Research Council (ERC) under the European Union’s Horizon 2000 research and innovation program (grant no.101042634).

AUTHOR CONTRIBUTIONS

A.B-A developed and optimized the protocols described in this manuscript, designed and performed the experiments, analyzed data and wrote the manuscript. D.S.P developed and optimized some of the protocols described in this manuscript, designed and performed some of the experiments, contributed to drafting the manuscript and revised it for important intellectual content. S.C, B.B.J, M.B and N.B.W, designed and performed some of the experiments, and contributed to drafting the manuscript. V.O contributed intellectual content. A.A analyzed data, contributed to drafting the manuscript and revised it for important intellectual content. C.L.M acquired some of the funding and revised the manuscript for important intellectual content. K.E.G and R.P.D. supervised the study, acquired some of the funding and revised the manuscript for important intellectual content. All authors approved the final manuscript.

DECLARATION OF INTEREST

C.L.M. is a co-founder of Pluriomics B.V. (now Ncardia B.V.) and has advisory roles in HeartBeat.bio AG, Angios GmBH, Mogrify Limited and Sartorius AG. C.L.M. and R.P.D. declare previous research funding from Sartorius AG for an unrelated study. A.B-A, D.S.P, S.C, B.B.J, M.R.M.B, N.B.W, V.O, A.A and K.E.G declare no competing interests.

MATERIALS AVAILABILITY

All new plasmids generated in this study have been deposited on Addgene (https://www.addgene.org/browse/article/28252243/). The hiPSC lines are available under an MTA. Requests should be directed to Dr Richard P. Davis (r.p.davis@lumc.nl).

Figure 1

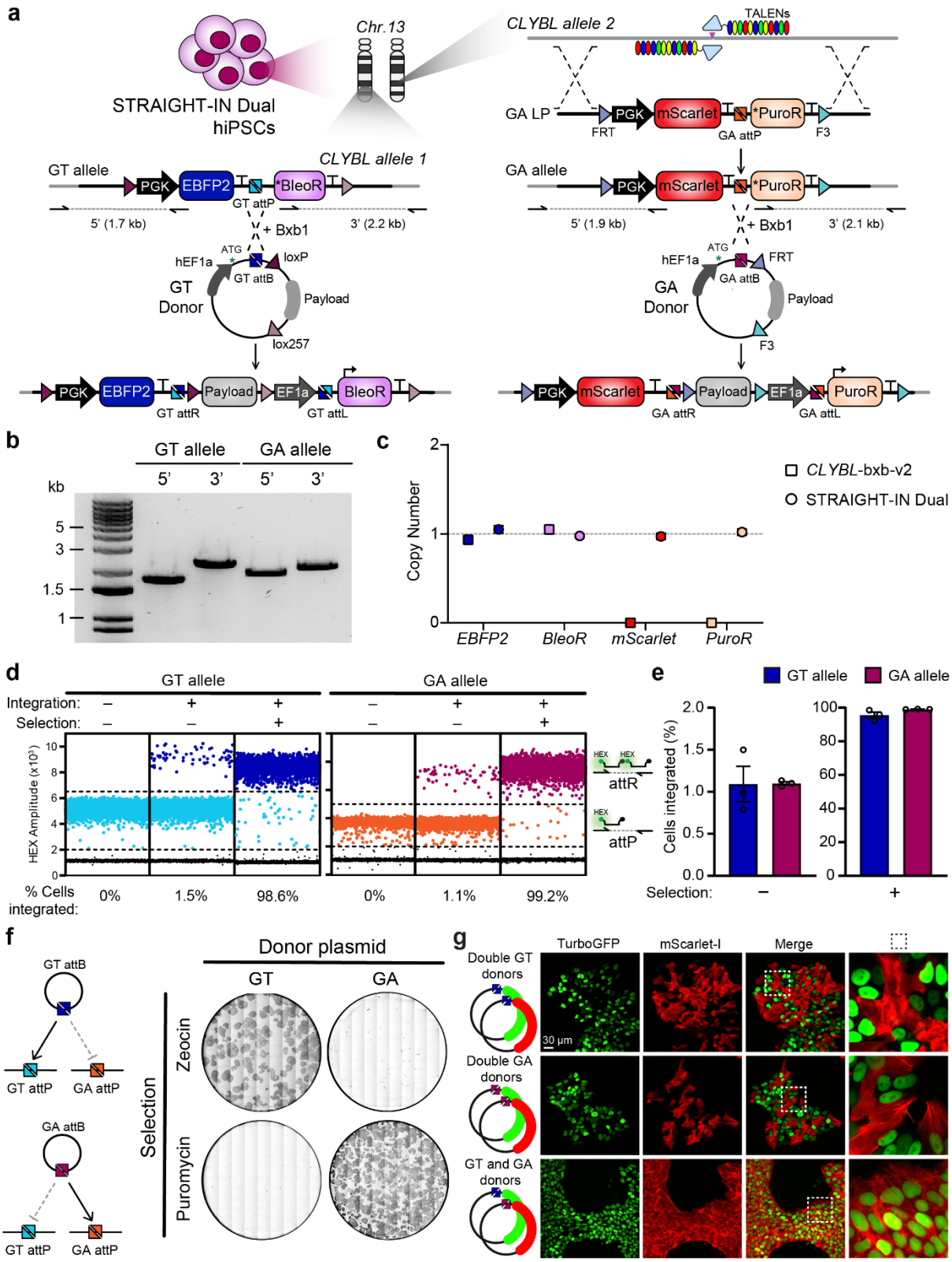
a
STRAIGHT-IN Dual hiPSCs
Chr.13
CLYBL allele 2
TALENs
GA LP
PGK
mScarlet
*PuroR
FRT
GA attP
F3
GT allele
CLYBL allele 1
EBFP2
*BleoR
GT attP
5' (1.7 kb)
3' (2.2 kb)
+ Bxb1
GA allele
5' (1.9 kb)
3' (2.1 kb)
ATG
hEF1a
loxP
GT attB
GT Donor
Payload
lox257
FRT
GA attB
GA Donor
F3
EF1a
BleoR
PuroR
GT attR
GT attL
GA attR
GA attL
b
GT allele
GA allele
5'
3'
kb
5
3
1.5
1
c
Copy Number
2
1
0
CLYBL-bxb-v2
STRAIGHT-IN Dual
EBFP2
BleoR
mScarlet
PuroR
d
GT allele
GA allele
Integration:
Selection:
HEX Amplitude (x10³)
attR
attP
% Cells integrated:
0%
1.5%
98.6%
0%
1.1%
99.2%
e
GT allele
GA allele
Cells integrated (%)
Selection:
f
GT attB
GT attP
GA attP
GA attB
Donor plasmid
GT
GA
Selection
Zeocin
Puromycin
g
TurboGFP
mScarlet-I
Merge
Double GT donors
Double GA donors
GT and GA donors
30 µm

Figure 1. Allele-specific targeting of bxb1-GT and bxb1-GA payloads in the STRAIGHT-IN Dual hiPSCs

(a) Schematic of TALEN-mediated targeting of the GA-LP cassette into the second allele of the citrate lyase beta-like (*CLYBL*) locus and Bxb1 recombinase-mediated integration of GT and GA donor plasmids into their cognate LPs. Expression of the antibiotic resistance markers is activated only upon correct donor plasmid integration, which supplies the missing initiation codon (*). Half arrows indicate junction PCR primer sites. “Payload” indicates the location of the desired DNA cargo for targeting in both the donor plasmid and following genomic integration. “T” denotes polyadenylation sequences.

(b) Junction PCR analysis confirming targeting of GT and GA LPs in the *CLYBL* locus.

(c) ddPCR validating single-copy genomic integration of each LP cassette. The *CLYBL*-bxb-v2 hiPSC line serves as a control. Error bars, Poisson 95% CI.

(d) Representative ddPCR dot plots showing GT and GA donor plasmid integration before and after antibiotic selection. Dots represent droplets containing the indicated sequence (*attR* or *attP*), with percentages showing the calculated integration efficiencies.

(e) Mean integration efficiencies of GT and GA donor plasmids before (-) and after (+) antibiotic selection. N=3 independent transfections; error bars, ±SEM.

(f) Schematic illustrating Bxb1-GT/GA recombination specificity (*left*), and alkaline phosphatase staining (*right*) confirming orthogonal payload integration at the GT and GA LPs.

(g) Fluorescence images showing allele-specific expression of TurboGFP (GT) and mScarlet-I (GA) following donor plasmid integration.

Figure 2

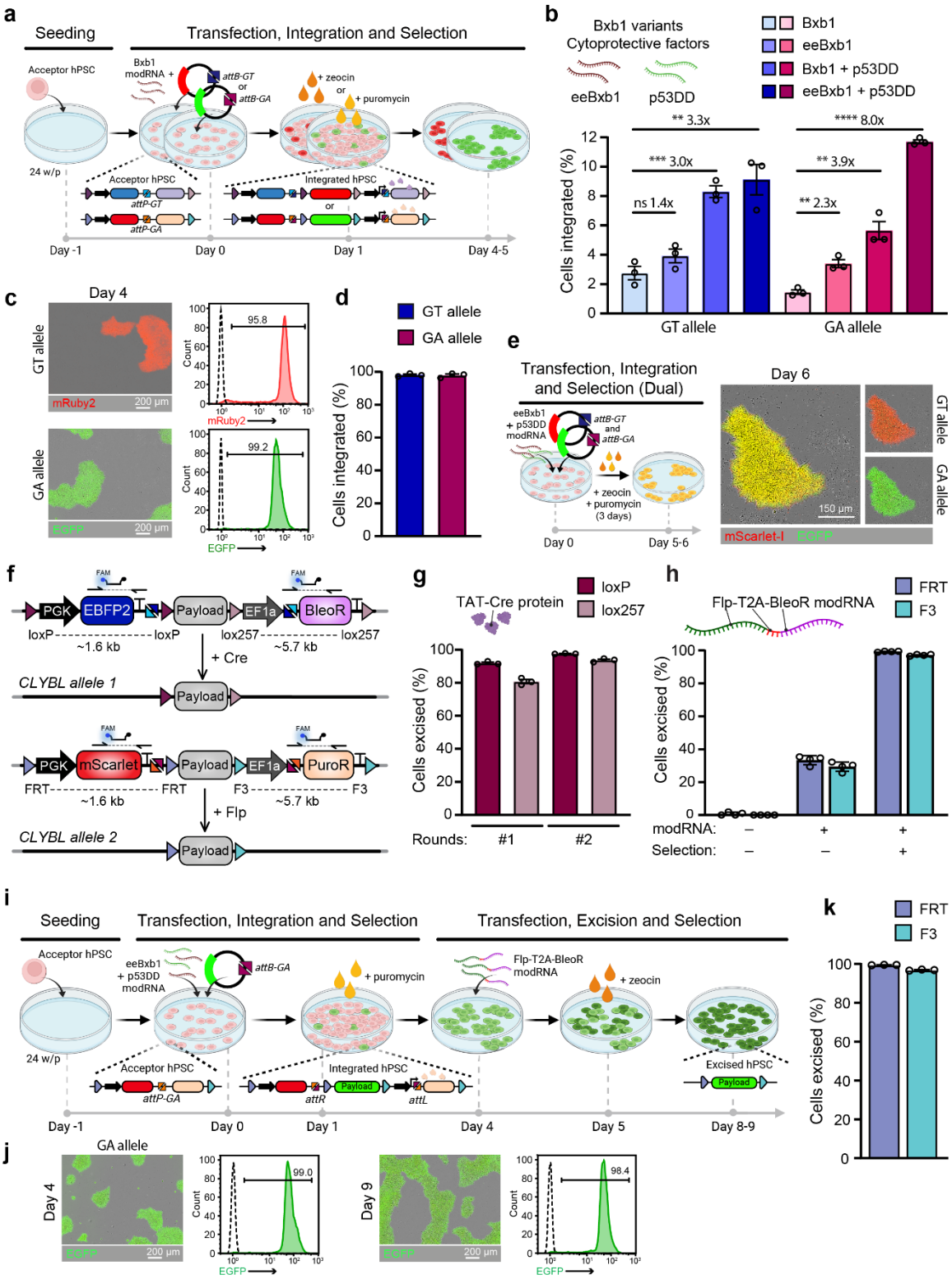
a
Seeding
Transfection, Integration and Selection
Acceptor hPSC
Bxb1 modRNA +
attB-GT or attB-GA
+ zeocin or + puromycin
24 w/p
Acceptor hPSC
attP-GT
attP-GA
Integrated hPSC
or
Day -1
Day 0
Day 1
Day 4-5
b
Bxb1 variants
Cytoprotective factors
eeBxb1
p53DD
Bxb1
eeBxb1
Bxb1 + p53DD
eeBxb1 + p53DD
** 3.3x
**** 8.0x
*** 3.0x
** 3.9x
ns 1.4x
** 2.3x
Cells integrated (%)
GT allele
GA allele
c
Day 4
GT allele
mRuby2
200 µm
95.8
Count
mRuby2
GA allele
EGFP
200 µm
99.2
EGFP
d
GT allele
GA allele
Cells integrated (%)
e
Transfection, Integration and Selection (Dual)
eeBxb1 + p53DD modRNA
attB-GT and attB-GA
+ zeocin + puromycin (3 days)
Day 0
Day 5-6
Day 6
150 µm
mScarlet-I
EGFP
GT allele
GA allele
f
PGK
EBFP2
Payload
EF1a
BleoR
FAM
loxP
~1.6 kb
loxP
lox257
~5.7 kb
lox257
+ Cre
CLYBL allele 1
Payload
PGK
mScarlet
Payload
EF1a
PuroR
FRT
~1.6 kb
FRT
F3
~5.7 kb
F3
+ Flp
CLYBL allele 2
Payload
g
TAT-Cre protein
loxP
lox257
Cells excised (%)
Rounds:
#1
#2
h
Flp-T2A-BleoR modRNA
FRT
F3
Cells excised (%)
modRNA:
Selection:
i
Seeding
Transfection, Integration and Selection
Transfection, Excision and Selection
Acceptor hPSC
24 w/p
eeBxb1 + p53DD modRNA
attB-GA
+ puromycin
Flp-T2A-BleoR modRNA
+ zeocin
Acceptor hPSC
attP-GA
Integrated hPSC
attR
Payload
attL
Excised hPSC
Payload
Day -1
Day 0
Day 1
Day 4
Day 5
Day 8-9
k
FRT
F3
Cells excised (%)
j
GA allele
Day 4
EGFP
200 µm
99.0
Count
EGFP
Day 9
EGFP
200 µm
98.4
Count
EGFP

Figure 2. Optimized STRAIGHT-IN protocol improved integration and excision efficiencies while reducing timelines

(a) Schematic of the rapid integration procedure.

(b) Mean integration efficiencies of GT and GA donor plasmids using modRNA combinations of Bxb1, eeBxb1 and p53DD prior to selection. N=3 independent transfections; error bars, ±SEM; not significant (ns), P>0.05; *, P≤0.05; **, P≤0.01; ***, P≤0.001; ****, P≤0.0001 (unpaired t test).

(c) Overlay of fluorescence and phase contrast images (*left*) and flow cytometry analysis (*right*) showing reporter expression following rapid integration of GT or GA donor plasmids encoding *mRuby2* or *EGFP*, respectively. Dashed lines denote untransfected STRAIGHT-IN Dual acceptor hiPSCs.

(d) Mean integration efficiencies of GT and GA donor plasmids following antibiotic selection. N=3 independent transfections; error bars, ±SEM.

(e) Schematic of the dual payload integration and selection procedure (*left*), and overlay of fluorescence and phase contrast images (*right*) after co-delivery of GT and GA donor plasmids encoding *mScarlet-I* and *EGFP*, respectively.

(f) Schematic for excising selection cassettes and plasmid backbones using Cre or Flp recombinases. Dashed lines indicate the sequences excised, and half arrows indicate primer sites for ddPCR analysis.

(g) Mean percentages of hiPSCs with indicated flanking regions excised following 1 (#1) or 2 (#2) administrations of TAT-Cre protein, as determined by ddPCR. N=3 independent transfections; error bars, ±SEM.

(h) Mean percentages of hiPSCs with indicated flanking regions excised following *Flp-2TA-BleoR* modRNA transfection, with (+) or without (-) zeocin selection, as determined by ddPCR. N=4 independent transfections; error bars, ±SEM.

(i) Schematic of the complete rapid integration and excision workflow.

(j) Representative fluorescence and phase contrast images, and flow cytometry analysis of hiPSCs transfected with a GA-*EGFP* donor plasmid on days 4 and 9 of the STRAIGHT-IN rapid integration and excision workflow. Dashed lines represent untransfected STRAIGHT-IN Dual acceptor hiPSCs.

(k) Mean percentage of hiPSCs with indicated flanking regions excised after *Flp-2TA-BleoR* modRNA transfection and zeocin selection, as determined by ddPCR. N=3 independent transfections; error bars, ±SEM.

Figure 3

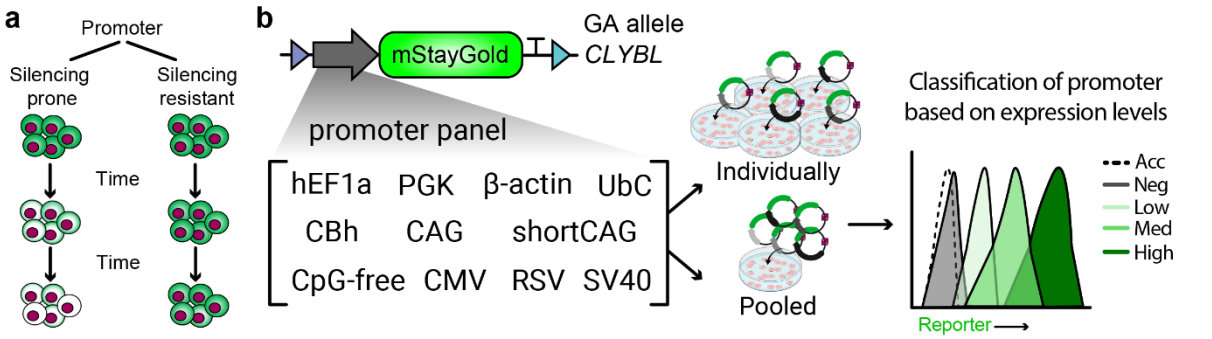
a
Promoter
Silencing prone
Silencing resistant
Time
Time
b
mStayGold
GA allele
CLYBL
promoter panel
hEF1a PGK β-actin UbC
CBh CAG shortCAG
CpG-free CMV RSV SV40
Individually
Pooled
Classification of promoter based on expression levels
Acc
Neg
Low
Med
High
Reporter

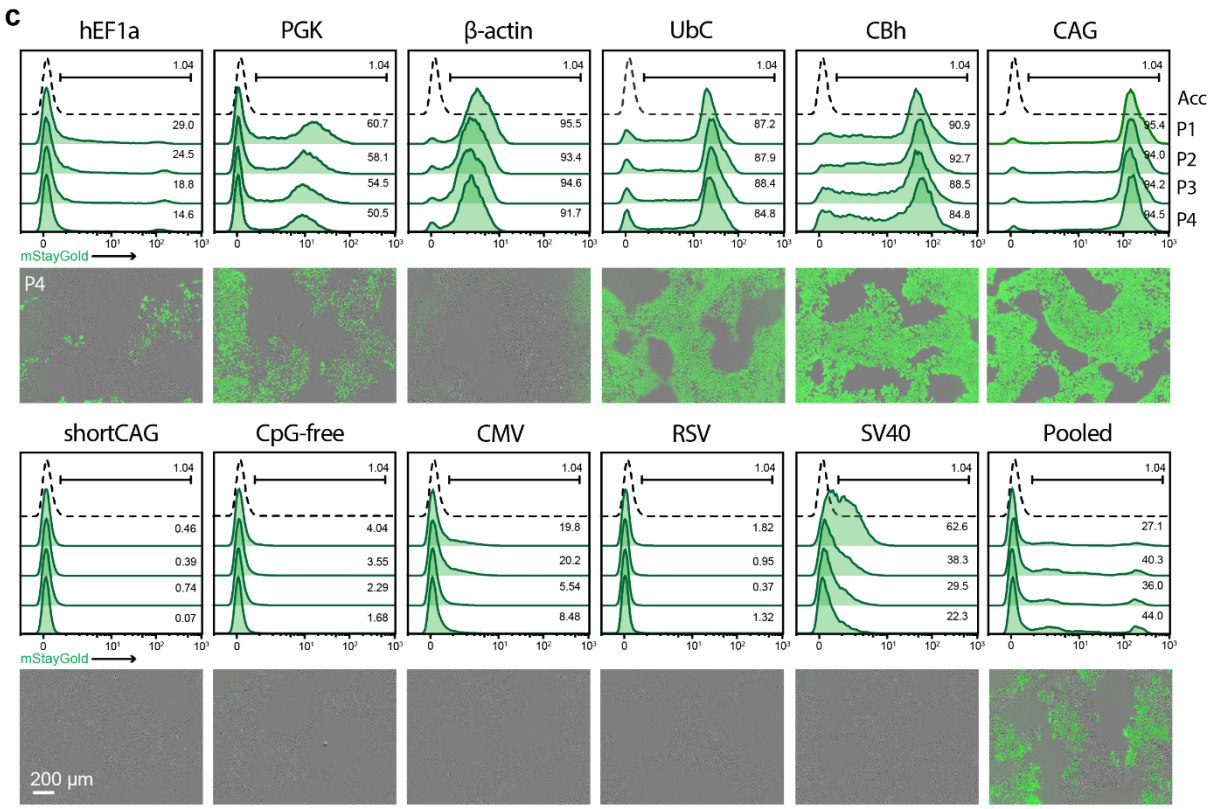
c
hEF1a
PGK
β-actin
UbC
CBh
CAG
shortCAG
CpG-free
CMV
RSV
SV40
Pooled
Acc
P1
P2
P3
P4
mStayGold
200 μm

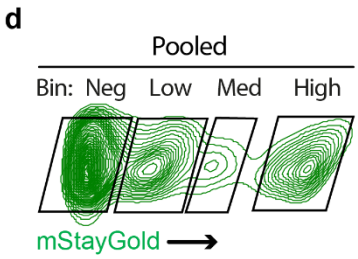
d
Pooled
Bin: Neg Low Med High
mStayGold

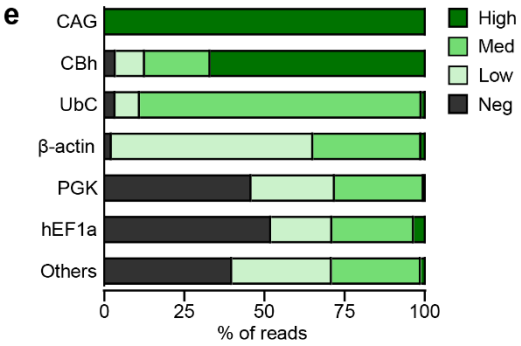
e
CAG
CBh
UbC
β-actin
PGK
hEF1a
Others
High
Med
Low
Neg
0
25
50
75
100
% of reads

Figure 3. Evaluation of transgene silencing using STRAIGHT-IN

(a) Conceptual schematic illustrating transgene silencing over time following genomic integration.

(b) Schematic of the panel of 11 different promoters, each driving expression of a *mStayGold* reporter integrated into the *CLYBL* locus. Donor plasmids were delivered either individually or as a pooled library to identify promoter sequences supporting high, medium and low transgene expression levels.

(c) Representative flow cytometry analysis (*top*), and overlaid fluorescence and phase-contrast images (*bottom*) over 4 passages of mStayGold expression in hiPSCs following individual promoter integration. Dashed lines indicate untransfected STRAIGHT-IN Dual acceptor hiPSCs.

(d) Flow cytometry analysis of the pooled integration approach, with the bulk population sorted into four mStayGold expression clusters: negative (neg), low, medium (med), and high.

(e) Bar graph showing the distribution of sequencing reads for the indicated promoter sequences mapping to each of the four expression clusters.

Figure 4

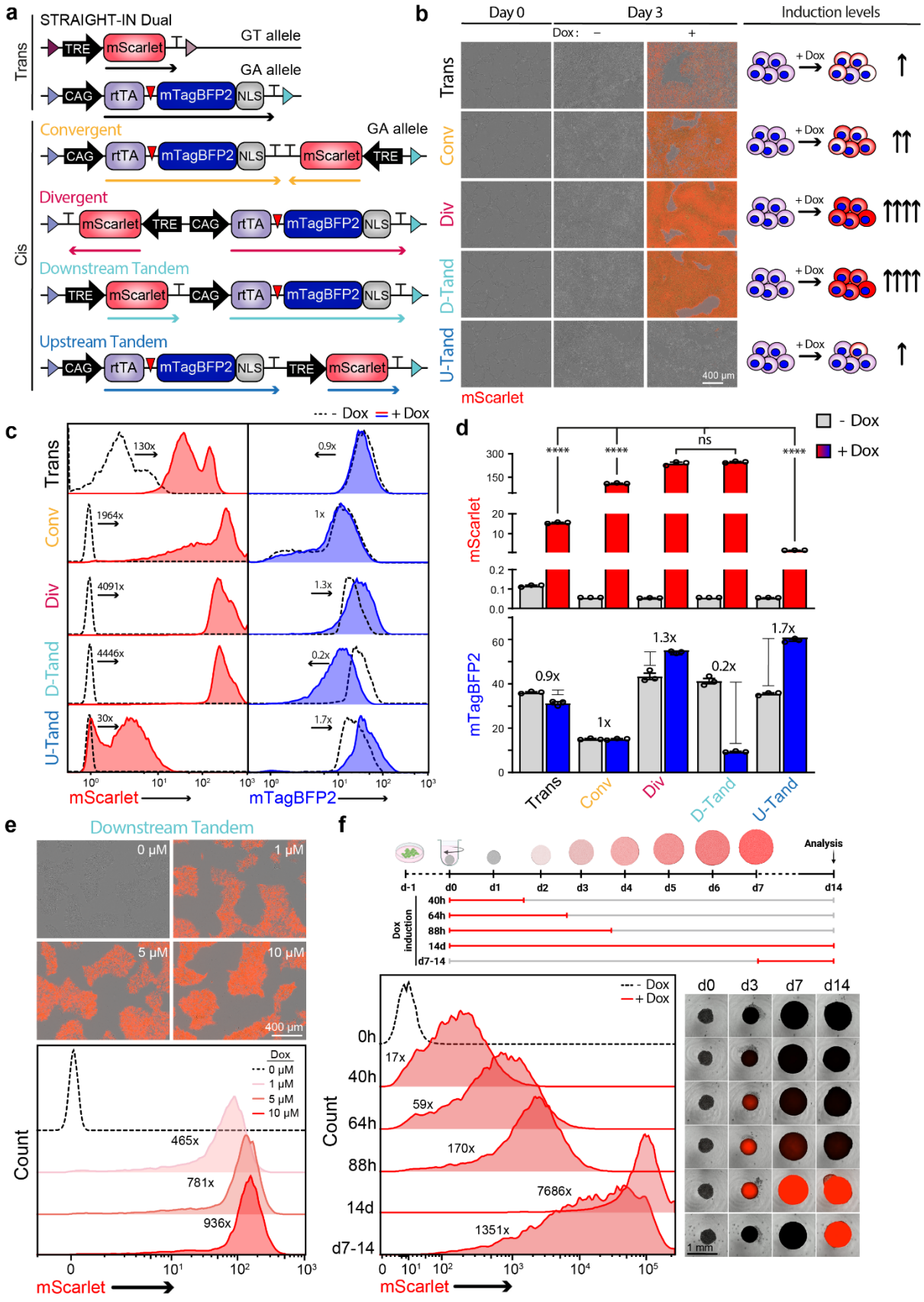
a
STRAIGHT-IN Dual
Trans
Cis
TRE
mScarlet
GT allele
GA allele
CAG
rtTA
mTagBFP2
NLS
Convergent
Divergent
Downstream Tandem
Upstream Tandem
b
Day 0
Day 3
Induction levels
Dox : – +
Trans
Conv
Div
D-Tand
U-Tand
+ Dox
400 µm
mScarlet
c
- Dox
+ Dox
130x
0.9x
1964x
1x
4091x
1.3x
4446x
0.2x
30x
1.7x
mScarlet
mTagBFP2
d
- Dox
+ Dox
****
ns
mScarlet
mTagBFP2
0.9x
1x
1.3x
0.2x
1.7x
Trans
Conv
Div
D-Tand
U-Tand
e
Downstream Tandem
0 µM
1 µM
5 µM
10 µM
400 µm
Dox
0 µM
1 µM
5 µM
10 µM
Count
465x
781x
936x
mScarlet
f
Analysis
d-1
d0
d1
d2
d3
d4
d5
d6
d7
d14
Dox induction
40h
64h
88h
14d
d7-14
- Dox
+ Dox
0h
40h
64h
88h
14d
d7-14
17x
59x
170x
7686x
1351x
Count
mScarlet
d0
d3
d7
d14
1 mm

Figure 4. Gene syntax modulates performance of the Tet-On 3G system in hiPSCs

(a) Schematic overview of a trans design and the four possible all-in-one Tet-On 3G syntaxes, defined by the relative orientation and order of the constitutive (*rtTA*-T2A-*mTagBFP2*) and doxycycline-inducible (TRE-*mScarlet*) transcriptional units. Arrows indicate transcriptional direction.

(b) Representative fluorescence/phase-contrast images (*left*) of hiPSCs carrying the integrated constructs shown in (**a**), cultured in the absence (-) or presence (+) of doxycycline for 3 days. The schematic (*right*) summarizes relative mScarlet expression across syntaxes.

(c) Flow cytometry analysis of mScarlet and mTagBFP2 expression in hiPSCs carrying each of the integrated constructs, in the absence (*dashed line*) or presence (*red*/*blue*) of doxycycline for 3 days. Values indicate fold change which is based on geometric mean fluorescence intensity (G-mean).

(d) Quantification of G-mean values for mScarlet and mTagBFP2 expression in the absence (*grey*) or presence (*red*/*blue*) of doxycycline for 3 days. N=3 biological replicates; mean ±SEM; ns, P>0.05; ****, P≤0.0001 (one-way ANOVA).

(e) Dose–response of doxycycline-induced mScarlet expression in hiPSCs harbouring the downstream tandem construct. Representative fluorescence/phase-contrast images (*top*) and flow cytometry analysis with values indicating fold changes based on the G-mean (*bottom*).

(f) Inducible mScarlet expression in cardioids carrying the downstream tandem construct. Schematic of the induction protocols (*top*). Flow cytometry analysis showing mScarlet expression in the absence (*dashed line*) or presence (*red*) of doxycycline for the indicated periods (*bottom left*). Fold change values (x) are based on the G-mean values relative to untreated cardioids. Representative fluorescence/phase-contrast images at different timepoints for the same indicated periods of doxycycline induction (*bottom right*).

Figure 5

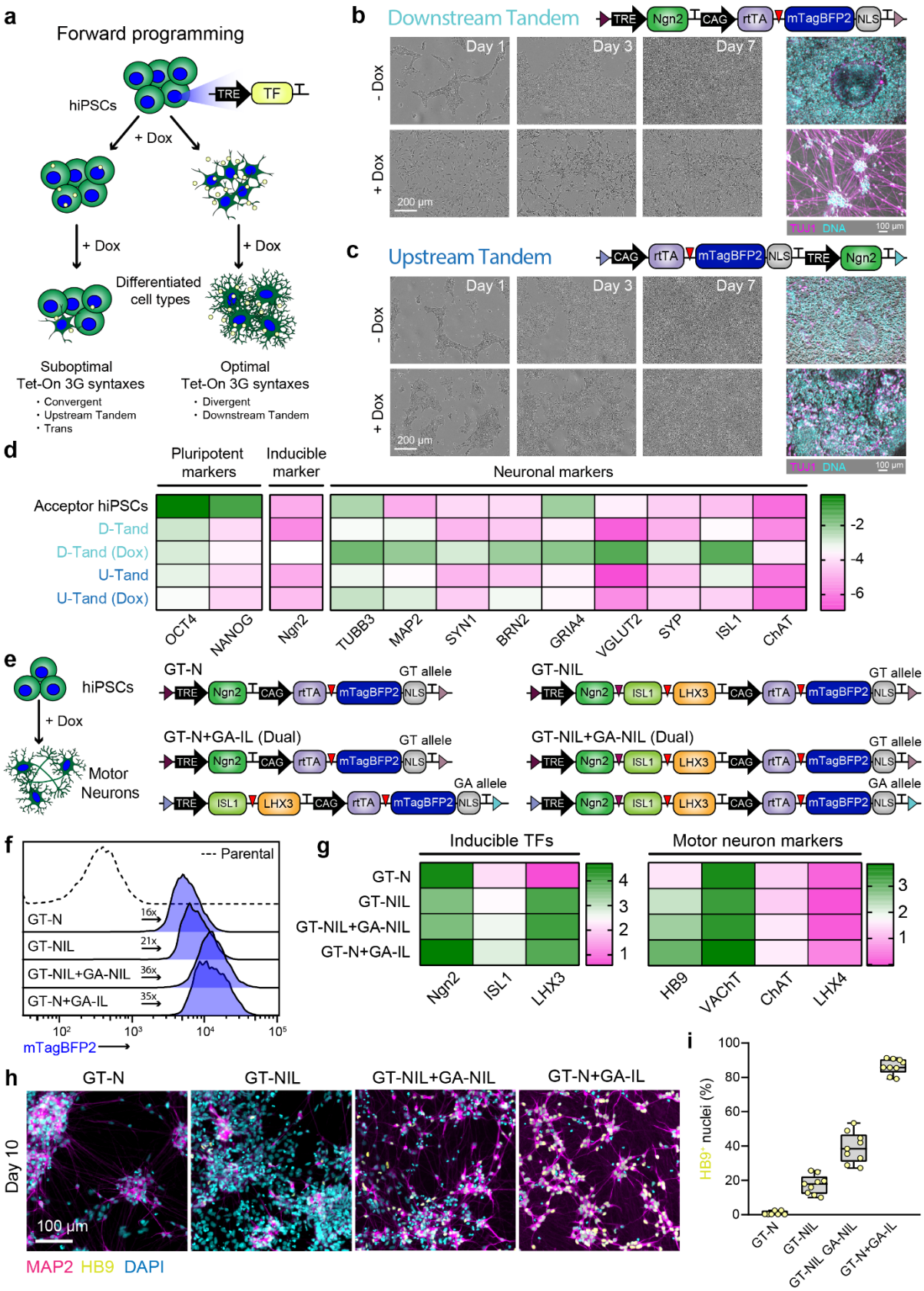
a
Forward programming
hiPSCs
TRE
TF
+ Dox
+ Dox
+ Dox
Differentiated cell types
Suboptimal Tet-On 3G syntaxes
• Convergent
• Upstream Tandem
• Trans
Optimal Tet-On 3G syntaxes
• Divergent
• Downstream Tandem
b
Downstream Tandem
TRE
Ngn2
CAG
rtTA
mTagBFP2
NLS
Day 1
Day 3
Day 7
- Dox
+ Dox
200 µm
TUJ1 DNA
100 µm
c
Upstream Tandem
CAG
rtTA
mTagBFP2
NLS
TRE
Ngn2
Day 1
Day 3
Day 7
- Dox
+ Dox
200 µm
TUJ1 DNA
100 µm
d
Pluripotent markers
Inducible marker
Neuronal markers
Acceptor hiPSCs
D-Tand
D-Tand (Dox)
U-Tand
U-Tand (Dox)
-2
-4
-6
OCT4
NANOG
Ngn2
TUBB3
MAP2
SYN1
BRN2
GRIA4
VGLUT2
SYP
ISL1
ChAT
e
hiPSCs
+ Dox
Motor Neurons
GT-N
GT allele
TRE
Ngn2
CAG
rtTA
mTagBFP2
NLS
GT-NIL
ISL1
LHX3
GT-N+GA-IL (Dual)
GA allele
GT-NIL+GA-NIL (Dual)
f
--- Parental
GT-N
16x
GT-NIL
21x
GT-NIL+GA-NIL
36x
GT-N+GA-IL
35x
mTagBFP2
g
Inducible TFs
Motor neuron markers
GT-N
GT-NIL
GT-NIL+GA-NIL
GT-N+GA-IL
Ngn2
ISL1
LHX3
HB9
VAChT
ChAT
LHX4
h
GT-N
GT-NIL
GT-NIL+GA-NIL
GT-N+GA-IL
Day 10
100 µm
MAP2 HB9 DAPI
i
HB9+ nuclei (%)
GT-N
GT-NIL
GT-NIL GA-NIL
GT-N+GA-IL

Figure 5. Doxycycline-inducible expression of multiple transcription factors using STRAIGHT-IN Dual

(a) Schematic of forward programming strategy to generate specific cell types by inducible overexpression of transcription factors.

(b) Schematic of a downstream tandem all-in-one doxycycline-inducible *Ngn2* cassette (*top*). Phase contrast and immunofluorescence images (TUJ1, magenta; DNA, cyan) of cells at indicated days treated with (+) or without (-) doxycycline (*bottom*).

(c) Schematic of an upstream tandem all-in-one doxycycline-inducible Ngn2 cassette (*top*), with corresponding images to those shown in **b** (*bottom*).

(d) Expression analysis of pluripotency and neuronal marker genes in untransfected hiPSCs and cells containing inducible *Ngn2* cassettes from **(b)** or **(c)**, treated with (+) or without (-) doxycycline for 7 days. Values are normalized to *RPL37A* and $\log_{10}$-transformed. N=3 independent differentiations.

(e) Schematic of representative single- and dual-cassette configurations tested for forward programming hiPSCs to iMNs.

(f) Flow cytometry analysis of mTagBFP2 expression in hiPSC lines with the indicated cassettes integrated in the GT or GA alleles. Dashed line represents untransfected STRAIGHT-IN Dual acceptor hiPSCs, with values indicating G-mean fold change relative to the untransfected parental cell line.

(g) Gene expression analysis of inducible transcription factors and motor neuron markers in cells containing the indicated single- or dual-cassette configurations and cultured with doxycycline for 10 days. Values are normalized to *RPL37A* and shown relative to uninduced conditions ($\log_{10}$-transformed). N=3 independent differentiations.

(h) Immunofluorescence images (MAP2, magenta; HB9, yellow; DNA, cyan) of the indicated cell lines treated with doxycycline for 10 days.

(i) Box plots showing the percentage of $HB9^+$ nuclei relative to $DAPI^+$ nuclei from images acquired as in (**h**).

Figure 6

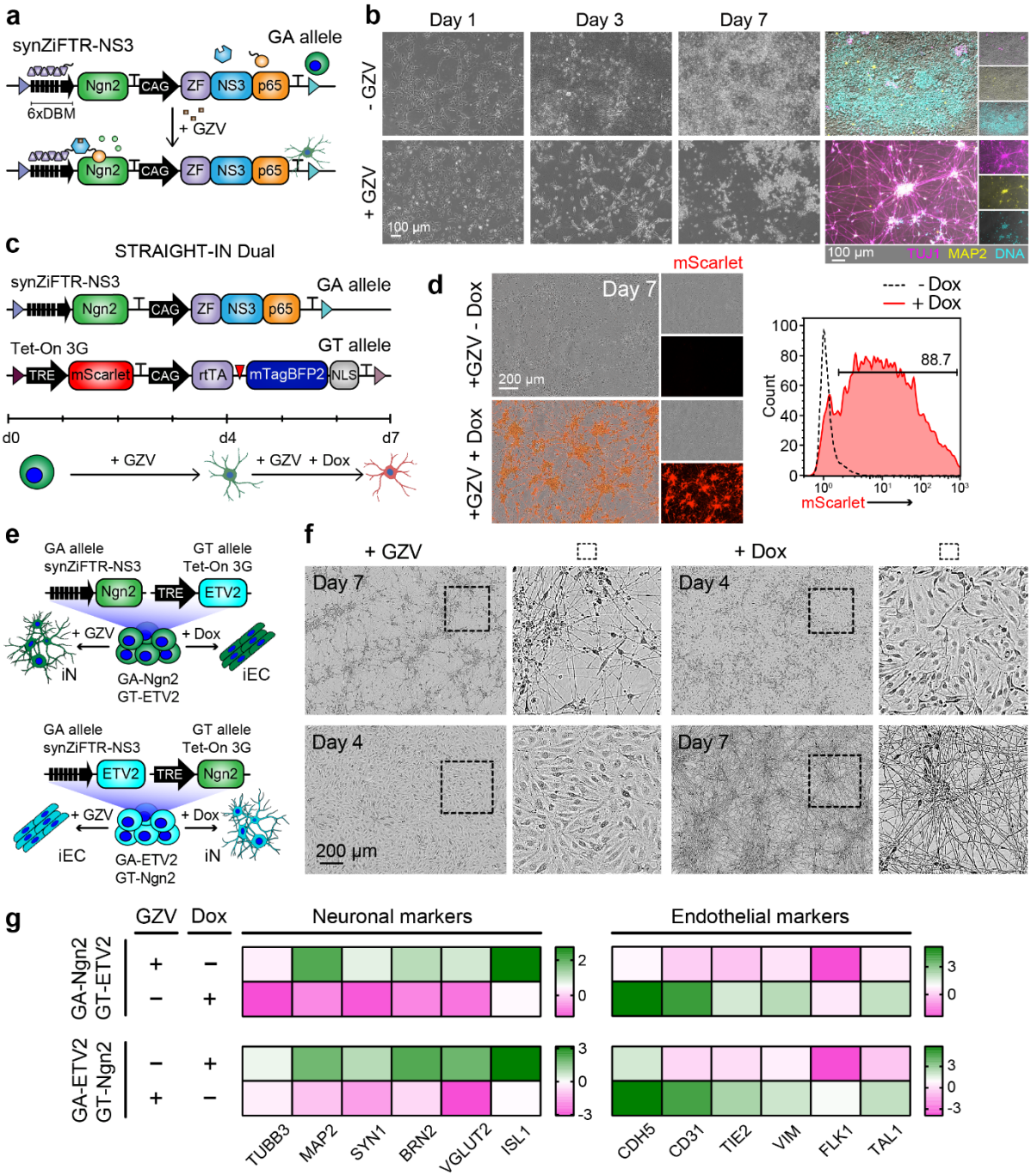
a
synZiFTR-NS3
GA allele
Ngn2
CAG
ZF
NS3
p65
6xDBM
+ GZV
b
Day 1
Day 3
Day 7
- GZV
+ GZV
100 µm
TUJ1 MAP2 DNA
c
STRAIGHT-IN Dual
Tet-On 3G
GT allele
TRE
mScarlet
rtTA
mTagBFP2
NLS
d0
d4
d7
+ GZV + Dox
d
mScarlet
+GZV - Dox
+GZV + Dox
200 µm
- Dox
+ Dox
Count
88.7
e
GA allele
synZiFTR-NS3
GT allele
Tet-On 3G
ETV2
iN
iEC
GA-Ngn2
GT-ETV2
GA-ETV2
GT-Ngn2
f
+ GZV
+ Dox
Day 7
Day 4
200 µm
g
GZV
Dox
Neuronal markers
Endothelial markers
TUBB3
MAP2
SYN1
BRN2
VGLUT2
ISL1
CDH5
CD31
TIE2
VIM
FLK1
TAL1

Figure 6. Dual-fate programming via orthogonal, inducible transcription factor expression using STRAIGHT-IN Dual

(a) Schematic of a downstream tandem synZiFTR-based *Ngn2* cassette integrated into the GA allele, enabling GZV-inducible expression.

(b) Phase contrast and immunofluorescence images of cells at indicated time points, cultured with (+) or without (-) GZV (TUJ1, magenta; MAP2, yellow; DNA, cyan).

(c) Schematic of STRAIGHT-IN Dual hiPSCs with a doxycycline-inducible *mScarlet* cassette in the GT allele and the GZV-inducible *Ngn2* cassette in the GA allele, enabling sequential and combinatorial induction.

(d) Representative fluorescence and phase contrast images (*left*), and flow cytometry analysis (*right*) of GZV-induced iNs cultured with (*red line*) or without (*dashed line*) doxycycline.

(e) Schematic of dual-fate STRAIGHT-IN Dual lines with all-in-one downstream tandem inducible *Ngn2* or *ETV2* cassettes regulated by synZiFTR (GA allele) or Tet-On 3G (GT allele) systems.

(f) Representative phase contrast images of hiPSC directed into iNs or iECs in the presence of either GZV or doxycycline for the indicated days.

(g) Gene expression analysis of neuronal and endothelial markers from the cells in (**f**). Values are normalized to *RPL37A* and shown relative to uninduced condition (log_{10}-transformed). N=3 independent differentiations.

METHODS

hiPSC line culture

All hiPSCs were maintained in StemFlex™ Medium (ThermoFisher) or mTeSR™ Plus Medium (STEMCELL Technologies) on tissue culture plates coated with Laminin-521 (BioLamina or STEMCELL Technologies) at 1.5 μg/cm^2. Cells were passaged twice weekly using either 1x TrypLE Select (ThermoFisher) or Gentle Cell Dissociation Reagent (STEMCELL Technologies).

Construction of Bxb1-GA LP targeting plasmid

To generate the *CLYBL*-Bxb1-LP-Dual-TC plasmid (Addgene, #229776), the *CLYBL*-Bxb1-LP-v2-TC plasmid (Addgene, #194327) was first digested with NheI and PmeI (both NEB). A LP fragment (composed of an *FRT* site, PGK promoter, *mScarlet* reporter, *attP*-GA site, a puromycin resistance gene lacking an initiation codon (**PuroR*) and a *F3* site) was PCR amplified from a separate plasmid source. The *CLYBL* R-HA homology arm fragment was PCR amplified from the *CLYBL*-Bxb1-LP-v2-TC plasmid. All components were amplified using PrimeSTAR® Max DNA Polymerase (Takara Bio), treated with DpnI (NEB), purified using the Wizard® SV Gel and PCR Clean-Up System kit (Promega) and assembled using the NEBuilder® HiFi DNA Assembly Cloning kit (NEB).

Generation of STRAIGHT-IN Dual hiPSC line

To generate the STRAIGHT-IN Dual hiPSC line (**Supplementary Figure 15)**, the GA-specific LP plasmid (*CLYBL*_Bxb1-GA_LP_Dual_TC) was targeted to the second allele of the *CLYBL* locus in LU99_*CLYBL*-bxb-v2 hiPSCs (LUMCi004-A-2). A total of 500 ng of the targeting plasmid and 500 ng each of the TALEN expression vectors pZT-C13-L1 and pZT-C13-R1 (Addgene #62196 and #62197)(Cerbini et al., 2015) were co-transfected using Lipofectamine™ Stem Transfection Reagent (ThermoFisher), according to the manufacturer's instructions.

Following recovery and expansion, mScarlet$^+$ cells were clonally isolated using the single-cell deposition function of a BD FACSAria III (BD Bioscience). The hiPSC clones were expanded and putative targeted clones (52/54, 94.5% targeting efficiency) were identified by PCR screening over the 5' junction as previously described (Blanch-Asensio et al., 2022). Targeting was further validated by PCR screening of the 3' junction, and by Sanger sequencing. Primer sequences are listed in **Supplementary Table 1**.

The LU99_*CLYBL*-bxb-v3_Dual hiPSC line (STRAIGHT-IN Dual; hPSCreg: LUMCi004-A-8) was

assessed for: (i) pluripotency marker expression; (ii) trilineage differentiation potential; (iii) mycoplasma contamination; and (iv) genomic integrity by G-banding karyotype analysis as well as with the iCS-digital™ PSC 24-probes kit (Stemgenomics). For G-band karyotyping, 20 metaphase spreads were examined with samples of sufficient quality to detect numerical and large structural abnormalities. Alkaline phosphatase staining was performed using the Alkaline Phosphatase Detection Kit (Merck) according to the manufacturer's instructions.

Donor plasmid assembly

Donor plasmids containing fluorescent reporters were assembled with isothermal cloning using the NEBuilder® HiFi DNA Assembly Cloning kit (NEB) or Golden Gate (Weber et al., 2011) cloning, as previously described (Blanch-Asensio et al., 2024; Kabaria et al., 2024; Love et al., 2025). Briefly, for payloads that were overexpressed using the Tet-On 3G system, the Bxb1-GT_AIO-TetOn_Down-Tandem Donor plasmid (Addgene, #229783) was digested with NotI (NEB), the genes of interest (GOIs) were PCR-amplified from other sources and assembled into the digested donor using the NEBuilder® HiFi DNA Assembly Cloning kit. Blue-white screening was performed by adding X-Gal (20 mg/mL, ThermoFisher) into the LB agar plate. A similar strategy was applied for the synZiFTR donor plasmid (Bxb1-GA_AIO-GZV-SynZiFTR_Down-Tandem donor; Addgene #229787). This plasmid was assembled using the NEBuilder® HiFi DNA Assembly Cloning kit from DNA fragments that were PCR-amplified from the pMN-334 plasmid (Addgene #195468)(H.-S. Li et al., 2022). For the promoter panel, the promoter sequences were PCR-amplified from the following plasmids: CMV (Addgene #40651), SV40 (Addgene #229779), RSV (Addgene #12253), PGK (Addgene #229776), CpG-free (Addgene #96945), shortCAG (Addgene #238347), hEF1a (Addgene #229779), CAG (Addgene #229790), UbC (Addgene #20342), CBh (Addgene #62988) and β-actin (Addgene #13680). The amplified promoter fragments were then cloned upstream of mStayGold in a linearized donor vector using the NEBuilder® HiFi DNA Assembly Cloning kit or Golden Gate cloning.

***In vitro* transcription**

The plasmid templates used for modRNA synthesis contained the 5'-UTR of human β-globin, a Kozak sequence, the coding sequences for the associated protein products, and the 3'-UTR of human β-globin. Linear templates used for *in vitro* transcription (IVT) were generated via PCR using Q5 DNA Polymerase (New England Biolabs) using a forward primer (5'-

AGCTATAATACGACTCACTATAAGctcctgggcaacgtgctg-3'), which encoded the T7 promoter compatible with the CleanCap AG reagent (upper-case bases, TriLink BioTechnologies) and annealed to the 5' UTR located on the plasmid template (lower-case bases) and a reverse primer (5'-poly(T)$_{116}$-GCAATGAAAATAAATGTTTTTTATTAGGCAGAAT-3'), which encoded the polyA sequence and annealed to the 3'-UTR on the plasmid template. PCR products were isolated from a 1% agarose gel, excised, and purified using the Monarch PCR and DNA Cleanup Kit (New England Biolabs). 200 ng of a purified product was used as a template in a 20 µL IVT reaction using the HiScribe T7 High Yield RNA Synthesis Kit (New England Biolabs), substituting UTP with N1-methylpseudouridine-5'-phosphate (TriLink Biotechnologies) and co-transcriptionally capping with CleanCap Reagent AG. IVT reactions were incubated at 37 °C for 2-4 h, at which point reactions were diluted to 50 µL, treated with 2 µL DNase I (ThermoFisher), and incubated at 37 °C for an additional 30 min to degrade the IVT PCR template DNA. Synthesized modRNAs were column purified and eluted with 60 µL water using the 50 µg Monarch RNA Cleanup Kit (New England Biolabs). The RNA concentration was determined using a spectrophotometer and the full-length product verified on a native denaturing gel. All modRNAs were stored at -80 °C.

Donor plasmid integration and enrichment

Unless otherwise stated, donor plasmids (300 ng per cm^2) were co-transfected into the *CLYBL*-bxb-v3 Dual hiPSC line alongside 400 ng of either a Bxb1 expression plasmid (pCAG-NLS-HA-Bxb1; Addgene #51271)(Hermann et al., 2014) or Bxb1 modRNA, using Lipofectamine™ Stem Transfection Reagent.

Approximately 3-4 days after transfection, hiPSCs were harvested and reseeded (~5 x 10^5 cells per well) on 12 well-plates. The next day, either zeocin (15 µg/ml, ThermoFisher) or puromycin (1 µg/ml, Invivogen) was added to the culture medium for 3 days.

Donor plasmid integration was confirmed via ddPCR using the *attP/attB* v2 and v3 integration assays as previously described (Blanch-Asensio et al., 2024). For the STRAIGHT-IN rapid protocol, either zeocin (15 µg/ml) or puromycin (1 µg/ml) was added to the culture medium one day post-transfection and maintained for 3 days.

Auxiliary element excision

hiPSCs containing integrated DNA payloads were seeded at a density of 2×10^5 cells per well in 24-well plates. The following day, cells were transfected using Lipofectamine™ Stem Transfection Reagent with 400 ng of either StemMACS™ *Cre* Recombinase or StemMACS™ *Flp* Recombinase modRNA (both Miltenyi Biotec).

For Flp-mediated excision using Flp-2TA-BleoR modRNA, 500 ng were transfected per well, and selection with zeocin (15 µg/mL) was initiated 24 h post-transfection and maintained for 3 days. Alternatively, TAT-*Cre* protein (1 µM) was added to the culture medium 1 day after passaging and maintained for 24 h, as previously described (Blanch-Asensio et al., 2024).

Once the cells were ~80% confluent (~2-3 days after transfection), the hiPSCs were passaged and maintained. The hiPSCs that were not replated were collected for gDNA extraction.

Genomic DNA (gDNA) extraction

gDNA from hiPSCs cultured in 96 well-plates was extracted using QuickExtract™ (Lucigen). Briefly, the cells were resuspended in 30 µl of QuickExtract and incubated at 65°C for 15 min, followed by 68°C for 15 min and 98°C for 10 min. gDNA from hiPSCs cultured in 24 or 12 well-plates was extracted using the High Pure PCR Template Preparation Kit (Roche) or the DNeasy *Blood* & *Tissue Kit* (QIAGEN) according to the manufacturer's instructions.

Droplet digital PCR (ddPCR)

ddPCR was performed and analyzed using a thermocycler, the Q200 AutoDG and QX200™ Droplet Digital PCR System, and QuantaSoft software (all Bio-Rad) as previously described (Blanch-Asensio et al., 2024). For all reactions, ~100 ng of gDNA was digested with HindIII (NEB). For copy number assays, the autosomal gene *RPP30* was used as a reference. The primers and probes for the ddPCR assays are listed in **Supplementary Table 2**.

DNA library preparation, bead cleanup and NGS analysis

Integrated promoter sequences were PCR-amplified from 100 ng of genomic DNA using the NEBNext® High-Fidelity 2X PCR Master Mix (NEB). Primer sequences and corresponding annealing temperatures are listed in **Supplementary Table 3**. PCR cycling conditions were as follows: initial denaturation at 98°C (30 s); 14 cycles of 98°C (10 s), annealing at the specified temperature (30 s), and extension at 72°C (30 s); followed by a final extension at 72°C (2 min).

PCR products were purified using AMPure XP Beads (Beckman Coulter) at a 1:1 beads:sample volume ratio. Samples were incubated for 10 min at room temperature to allow binding, before placed on a magnetic stand for 5 min, after which the supernatant was removed. The samples were washed twice with 80% ethanol for 30 s each time. After brief centrifugation, excess ethanol was removed, and the beads air-dried on a magnetic stand for 10 min. The PCR products were eluted in nuclease-free water by incubating for 5 min, followed by magnetic separation for an additional 5 min.

A second PCR amplification was performed using Illumina TruSeq small RNA adapters under the same thermocycling conditions, with annealing at 60°C. Final libraries were cleaned up using two additional bead purifications at 1:1 and 0.9:1 beads:sample volume ratio, respectively. Libraries were sequenced on an Illumina MiSeq platform using 300 bp paired-end reads. Sequencing reads were aligned to a custom reference file containing all expected promoter amplicons using BWA-MEM (version 0.7.17) with default parameters. Read counts for each promoter were determined independently from Read 1 and Read 2, yielding highly concordant results.

Cardioid differentiation

Cardioids were generated as previously described (Hofbauer et al., 2021) with minor adaptations. Briefly, hiPSCs were harvested using 1x TrypLE Select Enzyme for 5 min at 37°C, and 5 x 10^4 cells/well were seeded in U-bottom 96-well ultra-low attachment plates (PrimeSurface) in 200 µL of mBEL medium (Campostrini et al., 2021) containing 4 µM CHIR99021 (Axon Medchem), 30 ng/ml FGF-2 (Miltenyi Biotec), 5 µM LY294002 (Tocris Bioscience), 50 ng/ml Activin A (Miltenyi Biotec), 10 ng/ml BMP4 (R&D systems) and 1 µg/ml human insulin (Gibco). This medium was also supplemented with 1x CEPT cocktail to improve cell viability (Chen et al., 2021). After 40 h, the cells were refreshed with 200 µL of mBEL medium containing 8 ng/ml FGF-2, 10 ng/ml BMP4, 10 µg/ml human insulin, 0.25 µM IWPL6 (Abmole), 5 µM XAV939 (Tocris Bioscience), 0.05 µM retinoic acid (Sigma-Aldrich). Cardioids were refreshed daily with this medium until day 7, when it was replaced with mBEL medium containing 8 ng/ml FGF-2, 10 ng/ml BMP4 and 10 µg/ml human insulin). From day 7, cardioids were maintained in mBEL medium containing 10 µg/ml human insulin with refreshment every other day. Doxycycline (1 µM, ThermoFisher) was added to the medium as specified in **Figure 4**F. On day 14, cardioids from the same conditions were pooled and a single-cell suspension

obtained by dissociating the cardioids with 5x TrypLE Select for 10 min at 37°C and filtering the cell suspension. Data was acquired using a MacsQuant VYB (Miltenyi Biotec).

Forward programming to neurons and motor neurons

All hiPSC lines were dissociated into single cells with Gentle Cell Dissociation Reagent or 1x TrypLE Select and plated in 24-well plates coated with Laminin 521, at a density of 2.5 x 10^4 cells per well. Forward programming toward neurons (iNs) was initiated on the day of passage as described elsewhere (Pawlowski et al., 2017). Briefly, induction was performed in DMEM/F12 containing L-glutamine (Corning), non-essential amino acids (100x, Gibco), N2 supplement (100x, Fisher Scientific), penicillin/streptomycin (100x, Fisher Scientific), and doxycycline (1 µM). After 2 days, the medium was changed to Neurobasal™ Medium (Gibco) supplemented with Glutamax™ supplement (100x, Gibco), non-essential amino acids, B27 supplement (50x, Gibco), N2 supplement, BDNF (10 ng/ml, Peprotech), NT3 (10 ng/ml, Peprotech), Penicillin/Streptomycin and doxycycline (1 µM). Forward programming using the synZiFTR inducible system was performed by adding grazoprevir (125 nM, MedChemExpress) for 7 days. Additionally, 40 µM EdU was added to the cells from day 3 for a period of 48 h.

Differentiation to motor neurons (iMNs) by forward programming was performed similarly, but with the cells treated with doxycycline (1 µM) for 10 days. For the GT-NIL line, 40 µM EdU was additionally required from day 3 until day 5.

Forward programming to endothelial cells

The hiPSCs were dissociated into single cells with 1x TrypLE Select and plated in 24-well plates coated with Laminin 521, at a density of 2.5 x 10^4 cells per well. Induction was initiated on the day of passage in human endothelial SFM medium (Invitrogen) containing human serum from platelet poor plasma (100x, Sigma-Aldrich), human FGF (20 ng/ml, Miltenyi Biotec), human VEGF (30 ng/ml, Miltenyi Biotec), Penicillin/Streptomycin (100x), and doxycycline (1 µM). Doxycycline was only added for the first 72 h. Forward programming using the synZiFTR inducible system was performed by adding grazoprevir (500 nM) instead of doxycycline for the first 3 days.

RNA extraction, cDNA synthesis, and RT-qPCR

RNA was extracted using the NucleoSpin RNA kit (Macherey-Nagel) and reverse transcribed with the iScript cDNA synthesis kit (Bio-Rad). Quantitative PCR mixtures were prepared using

the iQ SYBR Green Supermix (Bio-Rad) with the samples run on a CFX Opus 384 Real-Time PCR System (Bio-Rad). The results were analyzed using the delta cycle threshold method (ΔCt). CT values were normalized to the housekeeping gene *RPL37A* and $\log_{10}$ transformed. Sequences of primers used in this study are listed in **Supplementary Table 4**.

Flow cytometry analysis

Single cell suspensions of hiPSCs were obtained by dissociating the cells with 1x TrypLE Select and subsequently filtered to remove cell aggregates. Flow cytometry data was acquired using either MacsQuant VYB (Miltenyi Biotec) or *Attune™ NxT* (ThermoFisher) flow cytometers, and analyzed using FlowJo software (v. 10.2, FlowJo). An example of the gating strategy is shown in **Supplementary Figure 16**. For assessment of pluripotency markers, the hiPSCs were fixed and permeabilized using the FIX and PERM™ Cell Permeabilization Kit (ThermoFisher) and incubated with the conjugated antibodies OCT3/4-BV421, NANOG-PE and SSEA4-FITC (all BD Biosciences). For assessment of endothelial cell markers, cells were incubated with the conjugated antibodies CD144-FITC (1:50, Invitrogen, 53-1449-42) and CD31-APC (1:100, Invitrogen, 50-149-40), or CD144-PE (1:50, Miltenyi Biotec, 130-135-356) and CD31-FITC (1:50, Miltenyi Biotec, 130-117-390).

Immunocytochemistry staining

For the trilineage differentiation, the hiPSCs were seeded on 96-well imaging microplates (Corning) and the trilineage differentiation was performed using the STEMdiff™ Trilineage differentiation kit (STEMCELL Technologies) following the manufacturer's instructions. Differentiated cells were fixed using 4% paraformaldehyde (PFA, ThermoFisher) in phosphate buffered saline without Ca^{2+} and Mg^{2+} **(**$PBS^{-/-}$) at room temperature for 15 min, and permeabilized and blocked using 0.05% Triton X-100 (Merck) and 10% fetal calf serum in $PBS^{+/+}$. Subsequently, the cells were incubated overnight with the conjugated primary antibodies (all from Cell Signaling Technology). For endoderm these were anti-FOXA2 (1:500, 8186) and anti-GATA4 (1:200, 36966); for ectoderm were anti-Nestin (1:200, 33475) and anti-PAX6 (1:200, 60433); and for mesoderm were anti-Brachyury/T (1:200, 81694) and anti-Vimentin (1:400, 5741). The next day, the cells were incubated at room temperature for 5 min with DAPI (1 µg/mL, ThermoFisher). Images were acquired using an EVOS™ M7000 cell imaging system (ThermoFisher) at 20x magnification.

The iNs were fixed in 4% PFA/PBS$^{-/-}$ at 4°C for 1 h, followed by three PBS$^{-/-}$ washes. Fixed samples were then permeabilized and incubated with blocking solution (5% fetal bovine serum, 0.5% Tween-20 in PBS$^{-/-}$) at 4°C overnight. Primary antibodies were diluted in 250 µL blocking solution per well for a 24 well-plate and incubated with the fixed cells overnight at 4°C. The cells were washed three times with 1 mL PBS$^{-/-}$. Conjugated secondary antibodies also diluted in 250 µL blocking solution with 0.1 µg/mL DAPI were incubated with samples for 1 h at 4°C. Samples were then washed using the same method and imaged. The following primary antibody dilutions were used: goat anti-Choline acetyltransferase (ChAT) (1:500, Sigma-Aldrich, AB144P), rabbit anti-microtubule-associated protein 2 (MAP2) (1:500, Cell Signaling Technology, 4542), mouse anti-tubulin beta 3 (TUBB3/TUJ1) (1:500, Biolegend, 801201). The following conjugated secondary antibody dilutions were used: Alexa Fluor® 647 AffiniPure™ donkey anti-goat IgG (1:500, Jackson ImmunoResearch, 705-605-147), Alexa Fluor® 594 donkey anti-rabbit IgG (1:500, ThermoFisher, A-21207), and Alexa Fluor® 647 donkey anti-mouse IgG (1:500, ThermoFisher, A-31571). Samples were imaged and processed using a Keyence™ all-in-one fluorescence microscope BZ-X800. Briefly, a maximum-intensity projection across a z-stack for each fluorescent channel was used to create the final images.

The iMNs were fixed in 4% PFA/PBS$^{-/-}$ at RT for 10 min, washed once with PBS$^{-/-}$ and incubated for 5 min at RT with permeabilization solution (0.1% Triton X-100 in PBS$^{-/-}$). Cells were then incubated with blocking solution (1% bovine serum albumin in PBS$^{-/-}$) at RT for 1 h. Primary antibodies mouse anti-MNR2/HB9 (1:100, DSHB, 81.5C10) and rabbit anti-MAP2 (1:250, Cell Signaling Technology, 4542S) were diluted in 70 µL blocking solution per well for a 96 well-plate and incubated with the fixed cells overnight at 4°C. The cells were washed twice with 100 µL PBS$^{-/-}$. The conjugated secondary antibodies Alexa Fluor® 488 donkey anti-mouse IgG (1:300, ThermoFisher, A-21202) and Alexa Fluor® 647 donkey anti-rabbit IgG (1:300, ThermoFisher, A-31573) were diluted in 70 µL blocking solution with 0.1 µg/mL DAPI and incubated with the cells for 1 h at RT. Samples were then washed twice and imaged using the Dragonfly high-speed confocal microscope (ANDOR) at 40x magnification.

The iECs were fixed and stained as described above. The following primary antibody dilutions were used: sheep anti-hCD31 (PECAM-1) (1:200, R&D Systems, AF806) and mouse anti-hZO-1 (1:200, Invitrogen, 33-9100). The following conjugated secondary antibody dilutions were used: Alexa Fluor® 647 donkey anti-sheep IgG (1:300, Invitrogen, A21448) and Alexa Fluor®

488 donkey anti-mouse IgG (1:300, Invitrogen, A21202).

Live-cell imaging and calcium recordings

Live imaging of fluorescent reporter gene expression was performed using one of the following systems: the BZ-X810 all-in-one fluorescence microscope (Keyence) at 10x or 20x magnification, the Incucyte S3 live cell analysis system (Sartorius) at 10x magnification, or the Dragonfly high-speed confocal microscope at 40x magnification. For intracellular calcium recordings, 20-second time-lapse videos were acquired on day 9 using the BZ-X810 microscope at 10x magnification with a frame rate of 10 frames per second. Calcium transients were analyzed using ImageJ (NIH), and intensity traces were plotted from three user-defined regions of interest.

Viability imaging of iMNs

Live cell imaging of iMNs was performed using Calcein AM (Invitrogen). Cells were incubated with Calcein AM (5 µM) for 30 min at 37°C, followed by a $PBS^{-/-}$ wash step and imaged at 10x magnification using the EVOS Auto2 microscope (ThermoFisher). For nuclear and viability staining, iMNs were also incubated with Hoechst 33342 (5 µg/mL, Invitrogen) and propidium iodide (10 µg/mL, Merck) for 1 h at 37°C, washed with $PBS^{-/-}$, and imaged using the same microscope and settings.

Quantification of iMNs

The TWOMBLI plugin (Wershof et al., 2021) for ImageJ was adapted to quantify total dendritic area, the number of branching points, and the overall dendritic length of iMNs stained with Calcein AM. TWOMBLI identified dendritic extensions by mapping ridgelines revealed through thresholding of Calcein AM-stained images, using predefined parameters. The total mapped length was calculated as the sum of all masked fiber lengths within each image, while the number of branch points was defined as the count of fiber intersections per image.

In parallel, a custom CellProfiler pipeline was developed to identify Hoechst-stained nuclei (DNA, blue) and propidium iodide-stained nuclei (non-viable cells, red). Red nuclei were masked over blue nuclei to eliminate co-localized signals, allowing for accurate quantification of surviving (blue-only) nuclei. The percentage of surviving nuclei was calculated based on this filtered count. For quantification of HB9 and DAPI signals, a custom CellProfiler pipeline was developed to enhance low-intensity images, identify nuclei, and perform cell counting. RGB

images were separated into individual color channels, followed by intensity rescaling and a minor Gaussian blur to reduce noise. Nuclei were segmented from the rescaled images using intensity-based thresholding, enabling the separation of clustered objects. $HB9^+$ nuclei (red channel) were then masked over the DAPI signal (blue channel) to identify the $HB9^-$ population. The total number of $HB9^+$ nuclei was used to calculate the percentage of HB9-expressing cells per image.

Statistical analysis

Unless otherwise stated, data is presented as mean ± SEM. Statistical analysis was performed using GraphPad Prism 8 software (v8.2.0, GraphPad). Sample sizes and statistical analyses are reported in the figure legends.

REFERENCES

Anzalone, A. V., Gao, X. D., Podracky, C. J., Nelson, A. T., Koblan, L. W., Raguram, A., Levy, J. M., Mercer, J. A. M., & Liu, D. R. (2022). Programmable deletion, replacement, integration and inversion of large DNA sequences with twin prime editing. *Nature Biotechnology*, *40*(5), 731–740. https://doi.org/10.1038/s41587-021-01133-w

Balmas, E., Sozza, F., Bottini, S., Ratto, M. L., Savorè, G., Becca, S., Snijders, K. E., & Bertero, A. (2023). Manipulating and studying gene function in human pluripotent stem cell models. *FEBS Letters*, *597*(18), 2250–2287. https://doi.org/10.1002/1873-3468.14709

Bertero, A., Pawlowski, M., Ortmann, D., Snijders, K., Yiangou, L., De Brito, M. C., Brown, S., Bernard, W. G., Cooper, J. D., Giacomelli, E., Gambardella, L., Hannan, N. R. F., Iyer, D., Sampaziotis, F., Serrano, F., Zonneveld, M. C. F., Sinha, S., Kotter, M., & Vallier, L. (2016). Optimized inducible shRNA and CRISPR/Cas9 platforms for in vitro studies of human development using hPSCs. *Development*, *143*(23), 4405–4418. https://doi.org/10.1242/dev.138081

Blanch-Asensio, A., Grandela, C., Brandão, K. O., de Korte, T., Mei, H., Ariyurek, Y., Yiangou, L., Mol, M. P. H., van Meer, B. J., Kloet, S. L., Mummery, C. L., & Davis, R. P. (2022). STRAIGHT-IN enables high-throughput targeting of large DNA payloads in human pluripotent stem cells. *Cell Reports Methods*, *2*(10), 100300. https://doi.org/10.1016/J.CRMETH.2022.100300

Blanch-Asensio, A., Grandela, C., Mummery, C. L., & Davis, R. P. (2024). STRAIGHT-IN: a platform for rapidly generating panels of genetically modified human pluripotent stem cell lines. *Nature Protocols*. https://doi.org/10.1038/s41596-024-01039-2

Blanch-Asensio, A., Vaart, B. Van Der, Vinagre, M., Groen, E., Arendzen, C., Freund, C., Geijsen, N., Mummery, C. L., & Davis, R. P. (2023). Generation of AAVS1 and CLYBL STRAIGHT-IN v2 acceptor human iPSC lines for integrating DNA payloads. *Stem Cell Research*, *66*, 102991. https://doi.org/10.1016/j.scr.2022.102991

Brandão, K. O., Brink, L. van den, Miller, D. C., Grandela, C., van Meer, B. J., Mol, M. P. H., de Korte, T., Tertoolen, L. G. J., Mummery, C. L., Sala, L., Verkerk, A. O., & Davis, R. P. (2020). Isogenic Sets of hiPSC-CMs Harboring Distinct KCNH2 Mutations Differ Functionally and in Susceptibility to Drug-Induced Arrhythmias. *Stem Cell Reports*, *15*(5), 1127–1139. https://doi.org/10.1016/j.stemcr.2020.10.005

Brosh, R., Laurent, J. M., Ordoñez, R., Huang, E., Hogan, M. S., Hitchcock, A. M., Mitchell, L. A., Pinglay, S., Cadley, J. A., Luther, R. D., Truong, D. M., Boeke, J. D., & Maurano, M. T. (2021). A versatile platform for locus-scale genome rewriting and verification. *Proceedings of the National Academy of Sciences of the United States of America*, *118*(10), 1–11. https://doi.org/10.1073/pnas.2023952118

Brown, A. J., Sweeney, B., Mainwaring, D. O., & James, D. C. (2014). Synthetic Promoters for CHO Cell Engineering. *Biotechnol. Bioeng*, *111*, 1638–1647. https://doi.org/10.1002/bit.25227/abstract

Cabrera, A., Edelstein, H. I., Glykofrydis, F., Love, K. S., Palacios, S., Tycko, J., Zhang, M., Lensch, S., Shields, C. E., Livingston, M., Weiss, R., Zhao, H., Haynes, K. A., Morsut, L., Chen, Y. Y., Khalil, A. S., Wong, W. W., Collins, J. J., Rosser, S. J., … Deans, T. L. (2022). The sound of silence: Transgene silencing in mammalian cell engineering. *Cell Systems*, *13*(12), 950–973. https://doi.org/10.1016/j.cels.2022.11.005

Campostrini, G., Meraviglia, V., Giacomelli, E., van Helden, R. W. J., Yiangou, L., Davis, R. P., Bellin, M., Orlova, V. V., & Mummery, C. L. (2021). Generation, functional analysis and applications of isogenic three-dimensional self-aggregating cardiac microtissues from human pluripotent stem cells. *Nature Protocols*, *16*(April), 2213–2256. https://doi.org/10.1038/s41596-021-00497-2

Cerbini, T., Funahashi, R., Luo, Y., Liu, C., Park, K., Rao, M., Malik, N., & Zou, J. (2015). Transcription activator-like effector nuclease (TALEN)-mediated CLYBL targeting enables enhanced transgene expression and one-step generation of dual reporter human induced pluripotent stem cell (iPSC) and neural stem cell (NSC) lines. *PLoS ONE*, *10*(1), 1–18. https://doi.org/10.1371/journal.pone.0116032

Chen, Y., Tristan, C. A., Chen, L., Jovanovic, V. M., Malley, C., Chu, P. H., Ryu, S., Deng, T., Ormanoglu, P., Tao, D., Fang, Y., Slamecka, J., Hong, H., LeClair, C. A., Michael, S., Austin, C. P., Simeonov, A., & Singeç, I. (2021). A versatile polypharmacology platform promotes cytoprotection and viability of human pluripotent and differentiated cells. *Nature Methods*, *18*(5), 528–541. https://doi.org/10.1038/s41592-021-01126-2

Ding, Y., Tamhankar, S., Du, F., Christopherson, T., Schlueter, N., Cohen, J. R., Shusta, E. V., & Palecek, S. P. (2025). ETV2 Overexpression Promotes Efficient Differentiation of Pluripotent Stem Cells to Endothelial Cells. *Biotechnology and Bioengineering, 122*(7), 1914-1928. https://doi.org/10.1002/bit.28979

Dou, Y., Lin, Y., Wang, T. Y., Wang, X. Y., Jia, Y. L., & Zhao, C. P. (2021). The CAG promoter maintains high-level transgene expression in HEK293 cells. *FEBS Open Bio*, *11*(1), 95–104. https://doi.org/10.1002/2211-5463.13029

Duportet, X., Wroblewska, L., Guye, P., Li, Y., Eyquem, J., Rieders, J., Rimchala, T., Batt, G., & Weiss, R. (2014). A platform for rapid prototyping of synthetic gene networks in mammalian cells. *Nucleic Acids Research*, *42*(21), 13440–13451. https://doi.org/10.1093/nar/gku1082

Engreitz, J. M., Haines, J. E., Perez, E. M., Munson, G., Chen, J., Kane, M., McDonel, P. E., Guttman, M., & Lander, E. S. (2016). Local regulation of gene expression by lncRNA promoters, transcription and splicing. *Nature*, *539*(7629), 452–455. https://doi.org/10.1038/nature20149

Guichardaz, M., Bottini, S., Balmas, E., & Bertero, A. (2024). Overcoming the Silencing of Doxycycline-Inducible Promoters in hiPSC-derived Cardiomyocytes. *Open Research Europe*, *4*(266). https://doi.org/10.12688/openreseurope.19024.1

Haenebalcke, L., Goossens, S., Dierickx, P., Bartunkova, S., D'Hont, J., Haigh, K., Hochepied, T., Wirth, D., Nagy, A., & Haigh, J. J. (2013). The ROSA26-iPSC Mouse: A Conditional, Inducible, and Exchangeable Resource for Studying Cellular (De)Differentiation. *Cell Reports*, *3*(2), 335–341. https://doi.org/10.1016/j.celrep.2013.01.016

Haideri, T., Howells, A., Jiang, Y., Yang, J., Bao, X., & Lian, X. L. (2022). Robust genome editing via modRNA-based Cas9 or base editor in human pluripotent stem cells. *Cell Reports Methods*, *2*(9), 100290. https://doi.org/10.1016/j.crmeth.2022.100290

Haideri, T., Lin, J., Bao, X., & Lian, X. L. (2024). MAGIK: A rapid and efficient method to create lineage-specific reporters in human pluripotent stem cells. *Stem Cell Reports*, *19*(5), 744–757. https://doi.org/10.1016/j.stemcr.2024.03.005

Hermann, M., Stillhard, P., Wildner, H., Seruggia, D., Kapp, V., Sánchez-Iranzo, H., Mercader, N., Montoliu, L., Zeilhofer, H. U., & Pelczar, P. (2014). Binary recombinase systems for high-resolution conditional mutagenesis. *Nucleic Acids Research*, *42*(6), 3894–3907. https://doi.org/10.1093/nar/gkt1361

Hew, B. E., Gupta, S., Sato, R., Waller, D. F., Stoytchev, I., Short, J. E., Sharek, L., Tran, C. T., Badran, A. H., & Owens, J. B. (2024). Directed evolution of hyperactive integrases for site specific insertion of transgenes. *Nucleic Acids Research*, *52*(14), e64. https://doi.org/10.1093/nar/gkae534

Hofbauer, P., Jahnel, S. M., Papai, N., Giesshammer, M., Deyett, A., Schmidt, C., Penc, M., Tavernini, K., Grdseloff, N., Meledeth, C., Ginistrelli, L. C., Ctortecka, C., Šalic, Š., Novatchkova, M., & Mendjan, S. (2021). Cardioids reveal self-organizing principles of human cardiogenesis. *Cell*, *184*(12), 3299-3317.e22. https://doi.org/10.1016/j.cell.2021.04.034

Hosur, V., Low, B. E., & Wiles, M. V. (2022). Programmable RNA-Guided Large DNA Transgenesis by CRISPR/Cas9 and Site-Specific Integrase Bxb1. *Frontiers in Bioengineering and Biotechnology*, *10*, 910151. https://doi.org/10.3389/fbioe.2022.910151

Jillette, N., Du, M., Zhu, J. J., Cardoz, P., & Cheng, A. W. (2019). Split selectable markers. *Nature Communications*, *10*, 4968. https://doi.org/10.1038/s41467-019-12891-2

Johnstone, C. P., & Galloway, K. E. (2022). Supercoiling-mediated feedback rapidly couples and tunes transcription. *Cell Reports*, *41*(3), 111492. https://doi.org/10.1016/j.celrep.2022.111492

Johnstone, C. P., Love, K. S., Kabaria, S. R., Jones, R. D., Blanch-Asensio, A., Ploessl, D. S., Peterman, E. L., Lee, R., Yun, J., Oakes, C. G., Mummery, C. L., Davis, R. P., DeKosky, B. J., Zandstra, P. W., & Galloway, K. E. (2025). Gene syntax defines supercoiling-mediated transcriptional feedback. *BioRxiv*. *Published online January 19, 2025.* https://doi.org/10.1101/2025.01.19.633652

Joung, J., Ma, S., Tay, T., Geiger-Schuller, K. R., Kirchgatterer, P. C., Verdine, V. K., Guo, B., Arias-Garcia, M. A., Allen, W. E., Singh, A., Kuksenko, O., Abudayyeh, O. O., Gootenberg, J. S., Fu, Z., Macrae, R. K., Buenrostro, J. D., Regev, A., & Zhang, F. (2023). A transcription factor atlas of directed differentiation. *Cell*, *186*(1), 209–229. https://doi.org/10.1016/j.cell.2022.11.026

Jusiak, B., Jagtap, K., Gaidukov, L., Duportet, X., Bandara, K., Chu, J., Zhang, L., Weiss, R., & Lu, T. K. (2019). Comparison of Integrases Identifies Bxb1-GA Mutant as the Most Efficient Site-Specific Integrase System in Mammalian Cells. *ACS Synthetic Biology*, *8*(1), 16–24. https://doi.org/10.1021/acssynbio.8b00089

Kabaria, S. R., Bae, Y., Ehmann, M. E., Beitz, A. M., Lende-Dorn, B. A., Peterman, E. L., Love, K. S., Ploessl, D. S., & Galloway, K. E. (2024). Programmable promoter editing for precise control of transgene expression. *BioRxiv Published Online July 14, 2024.* https://doi.org/10.1101/2024.06.19.599813

Karbassi, E., Padgett, R., Bertero, A., Reinecke, H., Klaiman, J. M., Yang, X., Hauschka, S. D., & Murry, C. E. (2024). Targeted CRISPR activation is functional in engineered human pluripotent stem cells but undergoes silencing after differentiation into cardiomyocytes and endothelium. *Cellular and Molecular Life Sciences*, *81*(1), 95. https://doi.org/10.1007/s00018-023-05101-2

Kelkar, A., Zhu, Y., Groth, T., Stolfa, G., Stablewski, A. B., Singhi, N., Nemeth, M., & Neelamegham, S. (2020). Doxycycline-Dependent Self-Inactivation of CRISPR-Cas9 to Temporally Regulate On- and Off-Target Editing. *Molecular Therapy*, *28*(1), 29–41. https://doi.org/10.1016/j.ymthe.2019.09.006

Li, H.-S., Israni, D. V, Gagnon, K. A., Ann Gan, K., Raymond, M. H., Sander, J. D., Roybal, K. T., Keith Joung, J., Wong, W. W., & Khalil, A. S. (2022). Multidimensional control of therapeutic human cell function with synthetic gene circuits. *Science*, *378*(6625), 1227–1234. https://doi.org/10.1126/science.ade0156

Li, J., Li, Y., Pawlik, K. M., Napierala, J. S., & Napierala, M. (2020). A CRISPR-Cas9, Crelox, and Flp-FRT Cascade Strategy for the Precise and Efficient Integration of Exogenous DNA into Cellular Genomes. *CRISPR Journal*, *3*(6), 470–486. https://doi.org/10.1089/crispr.2020.0042

Li, M., Zhong, A., Wu, Y., Sidharta, M., Beaury, M., Zhao, X., Studer, L., & Zhou, T. (2022). Transient inhibition of p53 enhances prime editing and cytosine base-editing efficiencies in human pluripotent stem cells. *Nature Communications*, *13*(1), 6354. https://doi.org/10.1038/s41467-022-34045-7

Liu, Z., Chen, O., Wall, J. B. J., Zheng, M., Zhou, Y., Wang, L., Ruth Vaseghi, H., Qian, L., & Liu, J. (2017). Systematic comparison of 2A peptides for cloning multi-genes in a polycistronic vector. *Scientific Reports*, *7*(1). https://doi.org/10.1038/s41598-017-02460-2

Love, K. S., Johnstone, C. P., Peterman, E. L., Gaglione, S., Birnbaum, M. E., & Galloway, K. E. (2025). Model-guided design of microRNA-based gene circuits supports precise dosage of transgenic cargoes into diverse primary cells. *Cell Systems*, *16*(6), 101269. https://doi.org/10.1016/j.cels.2025.101269

Low, B. E., Hosur, V., Lesbirel, S., & Wiles, M. V. (2022). Efficient targeted transgenesis of large donor DNA into multiple mouse genetic backgrounds using bacteriophage Bxb1 integrase. *Scientific Reports*, *12*, 5424. https://doi.org/10.1038/s41598-022-09445-w

Matreyek, K. A., Stephany, J. J., & Fowler, D. M. (2017). A platform for functional assessment of large variant libraries in mammalian cells. *Nucleic Acids Research*, *45*(11), e102. https://doi.org/10.1093/nar/gkx183

Mitchell, L. A., McCulloch, L. H., Pinglay, S., Berger, H., Bosco, N., Brosh, R., Bulajic, M., Huang, E., Hogan, M. S., Martin, J. A., Mazzoni, E. O., Davoli, T., Maurano, M. T., & Boeke, J. D. (2021). De novo assembly and delivery to mouse cells of a 101 kb functional human gene. *Genetics*, *218*(1), iyab038. https://doi.org/10.1093/genetics/iyab038

Ng, A. H. M., Khoshakhlagh, P., Rojo Arias, J. E., Pasquini, G., Wang, K., Swiersy, A., Shipman, S. L., Appleton, E., Kiaee, K., Kohman, R. E., Vernet, A., Dysart, M., Leeper, K., Saylor, W., Huang, J. Y., Graveline, A., Taipale, J., Hill, D. E., Vidal, M., … Church, G. M. (2021). A comprehensive library of

human transcription factors for cell fate engineering. *Nature Biotechnology*, *39*(4), 510–519. https://doi.org/10.1038/s41587-020-0742-6

Niwa, H., Yamamura, K.-I., & Miyazaki, J.-I. (1991). Efficient selection for high-expression transfectants with a novel eukaryotic vector. *Gene*, *108*, 193–200. https://doi.org/10.1016/0378-1119(91)90434-D

O'Connell, R. W., Rai, K., Piepergerdes, T. C., Samra, K. D., Wilson, J. A., Lin, S., Zhang, T. H., Ramos, E. M., Sun, A., Kille, B., Curry, K. D., Rocks, J. W., Treangen, T. J., Mehta, P., & Bashor, C. J. (2023). Ultra-high throughput mapping of genetic design space. *BioRxiv. Published Online March 17, 2023.* https://doi.org/10.1101/2023.03.16.532704

Otomo, J., Woltjen, K., & Sakurai, H. (2023). Uniform transgene activation in Tet-On systems depends on sustained rtTA expression. *IScience*, *26*(10), 107685. https://doi.org/10.1016/j.isci.2023.107685

Pandey, S., Gao, X. D., Krasnow, N. A., McElroy, A., Tao, Y. A., Duby, J. E., Steinbeck, B. J., McCreary, J., Pierce, S. E., Tolar, J., Meissner, T. B., Chaikof, E. L., Osborn, M. J., & Liu, D. R. (2025). Efficient site-specific integration of large genes in mammalian cells via continuously evolved recombinases and prime editing. *Nature Biomedical Engineering, 9*, 22-39. https://doi.org/10.1038/s41551-024-01227-1

Patel, H. P., Coppola, S., Pomp, W., Aiello, U., Brouwer, I., Libri, D., & Lenstra, T. L. (2023). DNA supercoiling restricts the transcriptional bursting of neighboring eukaryotic genes. *Molecular Cell*, *83*(10), 1573-1587.e8. https://doi.org/10.1016/j.molcel.2023.04.015

Pawlowski, M., Ortmann, D., Bertero, A., Tavares, J. M., Pedersen, R. A., Vallier, L., & Kotter, M. R. N. (2017). Inducible and Deterministic Forward Programming of Human Pluripotent Stem Cells into Neurons, Skeletal Myocytes, and Oligodendrocytes. *Stem Cell Reports*, *8*(4), 803–812. https://doi.org/10.1016/j.stemcr.2017.02.016

Peterman, E. L., Ploessl, D. S., & Galloway, K. E. (2024). Accelerating Diverse Cell-Based Therapies Through Scalable Design. *Annual Review of Chemical and Biomolecular Engineering*, *15*, 267–292. https://doi.org/10.1146/annurev-chembioeng

Pinglay, S., Bulajić, M., Rahe, D. P., Huang, E., Brosh, R., Mamrak, N. E., King, B. R., German, S., Cadley, J. A., Rieber, L., Easo, N., Lionnet, T., Mahony, S., Maurano, M. T., Holt, L. J., Mazzoni, E. O., & Boeke, J. D. (2022). Synthetic regulatory reconstitution reveals principles of mammalian Hox cluster regulation. *Science* , *377*(6601), eabk2820. https://doi.org/10.1126/science.abk2820

Randolph, L. N., Bao, X., Zhou, C., & Lian, X. (2017). An all-in-one, Tet-On 3G inducible PiggyBac system for human pluripotent stem cells and derivatives. *Scientific Reports*, *7*(1), 1549. https://doi.org/10.1038/s41598-017-01684-6

Rieck, S., Sharma, K., Altringer, C., Hesse, M., Triantafyllou, C., Zhang, Y., Busskamp, V., & Fleischmann, B. K. (2024). Forward programming of human induced pluripotent stem cells via the ETS variant transcription factor 2: rapid, reproducible, and cost-effective generation of highly enriched, functional endothelial cells. *Cardiovascular Research, 120*(12), 1472-1482. https://doi.org/10.1093/cvr/cvae129

Roelle, S. M., Kamath, N. D., & Matreyek, K. A. (2023). Mammalian Genomic Manipulation with Orthogonal Bxb1 DNA Recombinase Sites for the Functional Characterization of Protein Variants. *ACS Synthetic Biology*, *12*(11), 3352–3365. https://doi.org/10.1021/acssynbio.3c00355

Rosenstein, A. H., Sambathkumar, R., Murareanu, B. M., Dhaliwal, N. K., Sun, F., Zhao, X., Dadvar, A., Al-Attar, R., Chai, A., Gulati, N., Yin, T., Nguyen, M., Serra, D., Devina, T., Gilbert, P., Kunath, T., Laflamme, M. A., Ogawa, S., Muffat, J., … Garton, M. (2024). FAST-STEM: A Human pluripotent stem cell engineering toolkit for rapid design-build-test-learn development of human cell-based therapeutic devices. *BioRxiv Published Online May 24, 2024.* https://doi.org/10.1101/2024.05.23.595541

Seczynska, M., Bloor, S., Cuesta, S. M., & Lehner, P. J. (2022). Genome surveillance by HUSH-mediated silencing of intronless mobile elements. *Nature*, *601*(7893), 440–445. https://doi.org/10.1038/s41586-021-04228-1

Shin, S. W., Min, H., Kim, J., & Lee, J. S. (2024). A Precise and Sustainable Doxycycline-Inducible Cell Line Development Platform for Reliable Mammalian Cell Engineering with Gain-of-Function Mutations. *Metabolic Engineering,86*, 12-28 . https://doi.org/10.1016/j.ymben.2024.09.004

Skylar-Scott, M. A., Huang, J. Y., Lu, A., Ng, A. H. M., Duenki, T., Liu, S., Nam, L. L., Damaraju, S., Church, G. M., & Lewis, J. A. (2022). Orthogonally induced differentiation of stem cells for the programmatic patterning of vascularized organoids and bioprinted tissues. *Nature Biomedical Engineering*, *6*(4), 449–462. https://doi.org/10.1038/s41551-022-00856-8

Uenaka, T., Napole, A. B., Saha, A. D., Sun, D., Singavarapu, A., Calzada, L., Chen, J., Erlebach, L., McQuade, A., Ramos, D., Rigamonti, A., Salazar, L., Samelson, A. J., Sedov, K., Welsh, N. J., Wild, K., Wu, Q., Arenas, E., Bassett, A. R., … Wernig, M. (2025). Prevention of Transgene Silencing During Human Pluripotent Stem Cell Differentiation. *BioRxiv Published Online April 11, 2025.* . https://doi.org/10.1101/2025.04.07.647695

Wang, N. B., Adewumi, H. O., Lende-Dorn, B. A., Beitz, A. M., O'Shea, T. M., & Galloway, K. E. (2025). Compact transcription factor cassettes generate functional, engraftable motor neurons by direct conversion. *Cell Systems, 16(*4), 101206. https://doi.org/10.1016/j.cels.2025.101206

Weber, E., Engler, C., Gruetzner, R., Werner, S., & Marillonnet, S. (2011). A modular cloning system for standardized assembly of multigene constructs. *PLoS ONE*, *6*(2), e16765. https://doi.org/10.1371/journal.pone.0016765

Wershof, E., Park, D., Barry, D. J., Jenkins, R. P., Rullan, A., Wilkins, A., Schlegelmilch, K., Roxanis, I., Anderson, K. I., Bates, P. A., & Sahai, E. (2021). A FIJI macro for quantifying pattern in extracellular matrix. *Life Science Alliance*, *4*(3). https://doi.org/10.26508/LSA.202000880

Xu, Z., Thomas, L., Davies, B., Chalmers, R., Smith, M., & Brown, W. (2013). Accuracy and efficiency define Bxb1 integrase as the best of fifteen candidate serine recombinases for the integration of DNA into the human genome. *BMC Biotechnology*, *13*, 1–17. https://doi.org/10.1186/1472-6750-13-87

Yanagi, T., Phen, S. F., Ayala, J., Aydin, D. E., Jaramillo, S., & Truong, D. M. (2025). Termination sequence between an inducible promoter and ubiquitous chromatin opening element (UCOE) reduces gene expression leakage and silencing. *Journal of Biological Engineering*, *19*(1). https://doi.org/10.1186/s13036-025-00499-8

Yarnall, M. T. N., Ioannidi, E. I., Schmitt-Ulms, C., Krajeski, R. N., Lim, J., Villiger, L., Zhou, W., Jiang, K., Garushyants, S. K., Roberts, N., Zhang, L., Vakulskas, C. A., Walker, J. A., Kadina, A. P., Zepeda, A. E., Holden, K., Ma, H., Xie, J., Gao, G., … Gootenberg, J. S. (2023). Drag-and-drop genome insertion of large sequences without double-strand DNA cleavage using CRISPR-directed integrases. *Nature Biotechnology*, *41*, 500–512. https://doi.org/10.1038/s41587-022-01527-4

Zhang, H., Lesnov, G. D., Subach, O. M., Zhang, W., Kuzmicheva, T. P., Vlaskina, A. V., Samygina, V. R., Chen, L., Ye, X., Nikolaeva, A. Y., Gabdulkhakov, A., Papadaki, S., Qin, W., Borshchevskiy, V., Perfilov, M. M., Gavrikov, A. S., Drobizhev, M., Mishin, A. S., Piatkevich, K. D., & Subach, F. V. (2024). Bright and stable monomeric green fluorescent protein derived from StayGold. *Nature Methods*, *21*(4), 657–665. https://doi.org/10.1038/s41592-024-02203-y

Zhang, M., Yang, C., Tasan, I., & Zhao, H. (2021). Expanding the Potential of Mammalian Genome Engineering via Targeted DNA Integration. *ACS Synthetic Biology*, *10*(3), 429–446. https://doi.org/10.1021/acssynbio.0c00576

Zhang, Y., Pak, C. H., Han, Y., Ahlenius, H., Zhang, Z., Chanda, S., Marro, S., Patzke, C., Acuna, C., Covy, J., Xu, W., Yang, N., Danko, T., Chen, L., Wernig, M., & Südhof, T. C. (2013). Rapid single-step induction of functional neurons from human pluripotent stem cells. *Neuron*, *78*(5), 785–798. https://doi.org/10.1016/j.neuron.2013.05.029